

---

# LAVA: Explainability for Unsupervised Latent Embeddings

---

**Ivan Stresec**

Delft University of Technology  
The Netherlands  
i.stresec@tudelft.nl

**Joana P. Gonçalves**

Delft University of Technology  
The Netherlands  
joana.goncalves@tudelft.nl

## Abstract

Unsupervised black-box models can be drivers of scientific discovery, but remain difficult to interpret. Crucially, discovery hinges on understanding the model output, which is often a multi-dimensional latent embedding rather than a well-defined target. While explainability for supervised learning usually seeks to uncover how input features are used to predict a target, its unsupervised counterpart should relate input features to the structure of the learned latent space. Adaptations of supervised model explainability for unsupervised learning provide either single-sample or dataset-wide summary explanations. However, without automated strategies of relating similar samples to one another guided by their latent proximity, explanations remain either too fine-grained or too reductive to be meaningful. This is especially relevant for manifold learning methods that produce no mapping function, leaving us only with the relative spatial organization of their embeddings. We introduce Locality-Aware Variable Associations (LAVA), a post-hoc model-agnostic method designed to explain local embedding organization through its relationship with the input features. To achieve this, LAVA represents the latent space as a series of localities (neighborhoods) described in terms of correlations between the original features, and then reveals reoccurring patterns of correlations across the entire latent space. Based on UMAP embeddings of MNIST and a single-cell kidney dataset, we show that LAVA captures relevant feature associations, with visually and biologically relevant local patterns shared among seemingly distant regions of the latent spaces.

## 1 Introduction

A pragmatic explanation can simply be defined as an answer to the question “why?” [1]. Traditional models, like Newton’s law of gravitation, constitute pragmatic explanations as they allow reasoning about observable phenomena through rigorous mathematical description. Similarly, stochastic phenomena that lend themselves well to statistical modeling, including linear regression, are explainable through probabilistic reasoning. For more complex problems such as facial recognition or protein structure prediction, expert-led modeling is superseded by machine learning (ML), where flexible model architectures and automated end-to-end optimization algorithms take center stage. ML has seen considerable progress and success in leveraging high-dimensional data for scientific discovery across fields like chemistry, mathematics, and biology [2–5]. However, even when ML models make reliable predictions or reflect observed phenomena, reasoning about their decisions is notoriously difficult as many ML models are “black boxes”: even with full decomposability, the complexity of the data and operations required to produce an output often exceeds what is practically comprehensible [6–8]. Limited insight into model behavior is a major barrier to wider adoption of ML for decision making, especially in critical areas such as healthcare and aviation [5, 9–11]. To improve the understanding of ML, the community uses either intrinsically interpretable but restrictive models, or *post-hoc* explainability methods that enable interpretation of black-box models [9, 10, 12–14].

The increasing popularity and complexity of black-box ML poses challenges to existing *post-hoc* explainability methods, exposing their shortcomings and creating a need for new solutions. At its core, *post-hoc* explainability aims to enable reasoning about the output of the model in terms of its treatment of the original input data. This information enables cross-referencing of model behavior with domain knowledge for further verification and assessment of model reliability, as well as mitigation of unwanted biases. Existing explainability methods cover a wide range of approaches, including feature or sample importance, anchors, counterfactual explanations, among others [14]. However, most have been developed to explain supervised learning models, whose output tends to be a well-defined target label or quantity. This ostensibly ignores unsupervised black-box learning strategies, which are designed to reveal latent structure with limited prior knowledge, and thus also contribute meaningfully to scientific discovery. Indeed, latent embeddings based on autoencoders, transformers, and diffusion models have shown effectiveness in various tasks [15–18], and serve as the basis of foundation models [19]. Similarly, manifold learning is prominently used in bioinformatics for data exploration, trajectory inference, cell type annotation, spatial domain identification, and multi-omics integration [18, 20–23].

Crucially, most unsupervised black-box models output multi-dimensional latent embeddings. Relating such dimensions to the input data is less straightforward, as the axes of the learned latent space do not correspond to known quantities and are therefore difficult to interpret [24]. Approaches for disentangled representations have shown mixed results, suggesting that latent dimensions cannot be explained independently from one another [24, 25]. As a result, it might be necessary for explainability of unsupervised black-box models to focus on relationships between input data and the relative spatial organization of the embeddings. Moreover, many manifold learning methods only produce representations of the samples in the learned latent space, without an underlying mapping function to embed new data [26]. This means that all information is contained exclusively within the embeddings, making the link between latent organization and original data crucial for reasoning about the underlying model.

Existing literature on explainability of unsupervised black-box latent embeddings is limited. Most notably, [24] introduce a framework adapting feature and sample importance methodology developed for supervised models to the unsupervised setting. This contribution importantly enables explanations for unsupervised models using a wide range of explainability methods. However, available methods yield either individual sample or dataset-wide summary explanations, which ignore the inherent organization of the latent embeddings and are likely too fine-grained or too global to meaningfully understand the underlying model. This is especially relevant as many black-box models are non-linear and seek to capture local structure in the original high-dimensional data. In fact, the popular t-SNE and UMAP manifold learning algorithms [27–29] explicitly aim to preserve local sample neighborhoods of the input space in a lower-dimensional latent space. We therefore argue that effective explainability of latent embeddings requires some strategy to relate samples to one another based on their organization or proximity in the latent space. Manifold learning methods specifically have been characterized in terms of neighborhood retention [30], and further analyzed to recommend ways of setting hyperparameters [18, 31–33]. While these studies offer insight into these methods, they do not provide information on how the embeddings relate to the original data. More manual approaches can relate spatial organization to original features [34], but rely on prior knowledge, metadata, or target features of interest, and are likely infeasible for higher-dimensional data.

In this work, we propose Locality-Aware Variable Associations (LAVA), a model-agnostic method to explain learned latent embeddings through relationships between the input features and the local latent spatial organization. To explain local structure, LAVA creates explanations based on localities: neighborhoods of sample embeddings across the latent space. Each latent locality is linked to the original data through a representation comprising all pairwise correlations between the original features, considering only the original samples belonging to that locality’s neighborhood. To reveal the consistency of local relationships between localities throughout the latent space, LAVA identifies modules of reoccurring subpatterns of feature correlations across localities. Experiments with LAVA reveal that neighborhoods of embeddings across a latent space can show distinct correlation patterns but also share subpatterns of correlation, and demonstrate that LAVA modules capture similar subpatterns between localities. We use LAVA to explain UMAP embeddings of both MNIST and single-cell kidney datasets, and showcase its ability to identify visually and biologically relevant modules of pixels and gene expression correlation, respectively.

## 2 Methodology

The LAVA method consists of three steps: (1) locality definition, (2) locality representation, and (3) module extraction (Figure 1). The first two steps create a reduced representation of the embeddings to explain, linking the latent and original spaces through local latent neighborhoods called localities, summarized by correlations of the original features. The third step uncovers structure preserved throughout the latent space, in the form of correlation subpatterns reoccurring across localities.

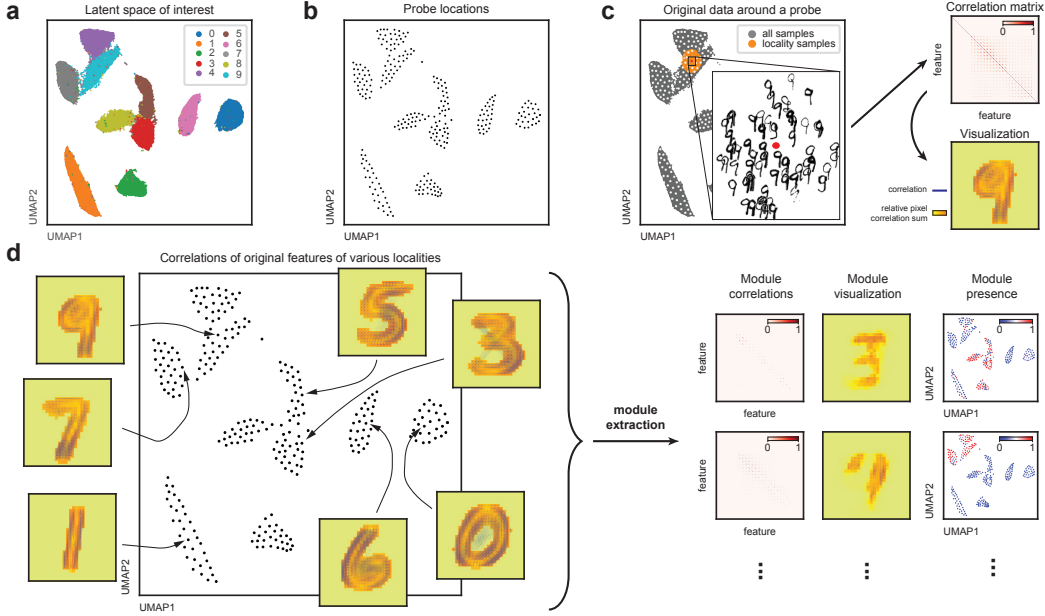


Figure 1: **LAVA method overview.** **a**, LAVA explains latent embeddings of a dataset (example UMAP embeddings of MNIST). **b**, Based on a neighborhood size hyperparameter  $k$ , LAVA represents the latent space as a series of localities: overlapping neighborhoods centered around latent points called probes. **c**, For each locality, LAVA calculates feature-to-feature correlations using the original samples of that locality (top right, locality correlations; bottom right, heatmap showing the sum of correlations per pixel, with added lines connecting correlated pixels). **d**, LAVA identifies modules yielding shared subpatterns of correlation across localities.

### 2.1 Locality Definition

To reflect the local structure of the input latent sample embeddings, LAVA uses a smaller number of localities centered around probe points (not samples) that are spread across the latent space (Figure 1b). The locality centered at probe  $p$  is then the  $n$ -sized Euclidean neighborhood containing the  $n$  neighbor samples nearest to  $p$  in the latent space. LAVA defines the number of localities  $\ell \leq E$  as  $\ell = E \times o/n$ , based on the number of input embeddings  $E$  and two hyperparameters: the neighborhood size  $n$ , and a factor  $o$  controlling the overlap between localities (Appendix A.1).

**Locality placement.** LAVA determines the placement of localities by optimizing locality in-degree centrality towards neighborhood in-degree centrality. In other words, by making the number of probe-based localities including a sample as a neighbor approximate, in relative terms, the number of  $n$ -neighborhoods including a sample as a neighbor out of all sample-based  $n$ -sized neighborhoods (Figures S5 and S11). Locality placement is optimized using weighted  $k$ -means clustering in combination with the DIRECT optimization algorithm [35, 36]: the goal is to find the locations of the  $\ell$  probes as cluster centers in  $k$ -means, with  $k = \ell$ , around which the  $\ell$  localities will be formed. Clustering is performed using the following sample weighting scheme:

$$w_i = \left( \frac{\text{in\_neighborhood}_i}{E} \right)^\alpha \times \left( \frac{1}{d_i^n} \right)^\beta, \quad (1)$$

where  $w_i$  is the weight of sample  $i$ ,  $in\_neighborhood_i$  is the in-degree centrality of sample  $i$  using sample-based  $n$ -neighborhoods,  $\bar{d}_i^n$  is the average distance from sample  $i$  to its  $n$  nearest neighbors, and  $\alpha$  and  $\beta$  are parameters optimized using the DIRECT algorithm (Appendix A.1). We define the cost function for DIRECT as the Manhattan distance between the neighborhood and locality in-degree centralities of each sample, as follows:

$$\mathcal{L}(\alpha, \beta) = \sum_{i=1}^E \left| \frac{in\_neighborhood_i}{E} - \frac{in\_locality_{i,\alpha,\beta}}{\ell} \right|, \quad (2)$$

where  $in\_locality_{i,\alpha,\beta}$  is the number of localities around the resulting  $\ell$  cluster centers that include  $i$  as a neighbor. Implementation details and pseudocode can be found in Appendix A.1.

## 2.2 Locality Representation

After defining localities, LAVA links the local structure of the latent space to the original data. This is achieved by representing each locality through pairwise associations between features, using only the samples within that locality in their original feature space. In this version of LAVA, feature association is defined as the absolute value of the Spearman correlation coefficient, capturing the strength of monotone association between features as values in  $[0, 1]$  (Figure 1c). Hence, the representation of each locality is a vector of  $\binom{D}{2}$  pairwise correlations for an original dataset with  $D$  features. Unlike Pearson correlations, Spearman correlations are not scale dependent and thus more flexible in the type of association they capture, while remaining computationally inexpensive and interpretable downstream. Individual correlations are filtered (set to 0) if one of the original features has the same value in  $> 75\%$  of the neighborhood (Appendix A.2).

## 2.3 Module Extraction

Finally, to reveal local relations preserved throughout the latent space, LAVA identifies modules of reoccurring feature association subpatterns across localities (Figure 2). Modules adhere to two properties: (1) modules capture reoccurring rather than average patterns across localities, since modules based on averages of localities would not be accurate representations of correlations observed at each locality individually; (2) modules can be co-present in the same locality, allowing decomposition of the locality pattern of correlation into subpatterns.

**Extraction.** Modules are identified based on the matrix of locality representations  $\mathbf{C}$ , with rows denoting the  $\ell$  localities and columns representing the  $\binom{D}{2}$  pairwise correlations. To identify modules, we propose the Association Matrix Factorization (AMF) method, which factorizes a matrix like  $\mathbf{C}$  into two: module matrix  $\mathbf{M}$  and presence matrix  $\mathbf{P}$ . The module matrix  $\mathbf{M}$  is of size  $M \times \binom{D}{2}$ , where each row represents one of  $M$  modules, columns denote correlations, and each row vector expresses a subpattern of correlations for the corresponding module. The presence matrix  $\mathbf{P}$  is of size  $\ell \times M$ , with each entry quantifying the presence of one of the  $M$  modules (or its subpattern) in one of the  $\ell$  localities. Both presence and module matrix entries are restricted to real values in  $[0, 1]$ , and they reconstruct the locality correlations using the maximum formulation described below.

### 2.3.1 AMF formulation

The formulation of AMF enables modules to overlap across localities. Crucially, as correlations or measures of associations more broadly cannot be considered additive, we avoid summing correlations and instead use a per element maximum function. This allows modules to contribute potentially overlapping subpatterns of correlations without direct interaction in the reconstruction. To that effect, we reconstruct each correlation  $j$  of each locality  $i$  by taking the maximum of the modules' corresponding correlation values multiplied by the presences of those module at locality  $i$ :

$$\hat{\mathbf{C}}_{ij} = \max \left( \mathbf{P}_i \odot (\mathbf{M}^T)_j \right), \quad (3)$$

where  $\odot$  is the Hadamard product and single letter subscripts indicate matrix rows. The reconstruction of the entire locality  $i$  can then be written as a per element maximum across products of the locality's presence values and the modules (Figure 2a):

$$\hat{\mathbf{C}}_i = \max_{1 \leq j \leq \binom{D}{2}} \left( \mathbf{P}_{i1} \times \mathbf{M}_1^T, \mathbf{P}_{i2} \times \mathbf{M}_2^T, \dots, \mathbf{P}_{iM} \times \mathbf{M}_M^T \right), \quad (4)$$

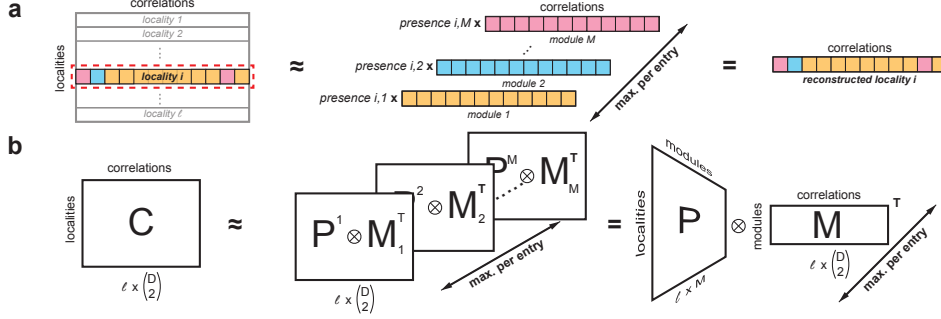


Figure 2: **Module-based factorization of localities.** **a**, A locality  $i$  is reconstructed by multiplying each module’s entries by the module presence for that locality, and then taking the maximum per entry across the  $M$  extracted modules. **b**, Localities are represented as a matrix  $C$ , where each row is a locality, each column a pair of original features, and each entry the pairwise feature correlation in that locality. Module extraction approximates  $C$  using a maximum per entry based on modules  $M$  and their presences  $P$ : it calculates an outer product between each column of  $P$  (superscript) and each row of  $M$ , yielding a tensor of  $M$  matrix slices of the same shape as  $C$  (Equation 5). Each slice represents a module’s contribution to the correlations of a locality. The  $M$  dimension is reduced by taking the per element maximum, yielding the reconstructed locality dataset.

where  $j$  is the index of a single correlation. Similarly, across all  $\ell$  localities, we can take the per element maximum of  $M$  matrices (Figure 2b), defined for some module  $m$  as:

$$P^m \otimes M_m^T = \begin{bmatrix} P_{1m} M_{m1} & P_{1m} M_{m2} & \dots & P_{1m} M_{m(\frac{D}{2})} \\ P_{2m} M_{m1} & P_{2m} M_{m2} & \dots & P_{2m} M_{m(\frac{D}{2})} \\ \vdots & \vdots & \ddots & \vdots \\ P_{\ell m} M_{m1} & P_{\ell m} M_{m2} & \dots & P_{\ell m} M_{m(\frac{D}{2})} \end{bmatrix}, \quad (5)$$

where the superscript  $m$  denotes the column of the matrix  $P$  (the presence vector of some module  $m$ ) and  $\otimes$  is the outer product. Intuitively, the reconstruction of all localities is similar to matrix multiplication between the presence matrix and the module matrix, but instead of summing up entries across the module dimension, we take their maximum. In tensor terminology, outer products from Equation 5 for each of the modules produce  $M$  slices of size  $\ell \times \binom{D}{2}$ , over which we take the per entry maximum to reconstruct the original locality matrix.

### 2.3.2 AMF loss function

To prevent averaging, rather than extraction of reoccurring subpatterns, we up-weight overestimation errors, similarly to quantile regression [37], but using a cosine distance instead of mean absolute error. We define the loss function for some locality  $i$  as:

$$\mathcal{L}(C_i, \hat{C}_i) = \frac{\|C_i\|_2}{\sum_{j \neq i} \|C_j\|_2} d_{\cos}(\mathbf{w}_i \odot C_i, \mathbf{w}_i \odot \hat{C}_i) + \gamma \text{MAE}(C_i, \hat{C}_i), \quad (6)$$

where  $\|\cdot\|_2$  are  $L2$  norms,  $\hat{C}_i$  is the locality reconstruction (Equation 4),  $\odot$  is the Hadamard product,  $d_{\cos}$  is cosine distance defined as  $d_{\cos}(\mathbf{x}, \mathbf{y}) = (1 - \cos(\mathbf{x}, \mathbf{y}))$ , MAE is the mean absolute error and  $\alpha$  the belonging regularization hyperparameter, and  $\mathbf{w}_i$  is an overestimation mask, defined as:

$$w_{ic} = \begin{cases} \nu, & \text{if } \hat{C}_{ic} > C_{ic} \\ 1, & \text{otherwise} \end{cases}, \quad (7)$$

where  $w_{ic}$  is the weight for locality  $i$  and correlation  $c$ , and  $\nu$  is an up-weighting hyperparameter (Appendix A.3). The cosine distance is the main term of the loss function, whose semantics we deem appropriate for module extraction because we are more concerned with patterns of correlations than their absolute values. The scale invariant cosine distance is scaled by a locality’s  $L2$  norm to focus on explaining localities showing many high correlations, as opposed to few correlations or mostly weak correlations. The MAE is a regularization term designed to match the scale of the original correlations. This allows for the evaluation of overestimation in the final solutions (Appendix A.3).

### 2.3.3 Deciding on the number of modules

We decide the number of modules similarly to an approach employed for non-negative matrix factorization (NMF) [38]. For a given number of modules  $M$ , we run the AMF method  $R$  times using different random initializations of matrices  $M$  and  $P$ . To assess the stability of the solution, we find  $M$ -medoids clusters using all  $R \times M$  modules and then calculate the silhouette width based on cosine similarity. A higher silhouette width indicates that similar modules were extracted across the different runs. We repeat this process for various values of  $M$ , and select a solution with a relatively low number of modules that provides a good trade-off between stability and accurate reconstruction. We argue that lower values of  $M$  are desirable, as they will force the optimization to find more global, shared patterns. However, too low a number might force different subpatterns to merge, which should also be reflected in poorer reconstructions. Once a number of modules is chosen, for the final modules, we select the run that has the lowest loss. We comment on limitations in Section 4.

## 3 Experiments

We perform experiments to verify and examine the explanations of LAVA. We first look at a latent space as represented by LAVA localities, and show how different local subpatterns of correlation can exhibit different levels of similarity across the latent space. Then, we look at how module extraction reveals and utilizes these similarities by extracting modules of reoccurring subpatterns, and verify their properties mentioned in Section 2. Finally, we use LAVA modules to explain a UMAP embedding of a kidney single-cell gene expression dataset, revealing biologically relevant patterns.

**Datasets** Our experiments are based on two datasets: MNIST handwritten digit images [39], and KPMP<sup>1</sup> single-cell kidney gene expression [40]. The KPMP dataset measures the activity of  $\sim 30k$  genes (features) for  $\sim 225k$  kidney cells (samples) [41]. **Experimental setup.** We use the following UMAP embeddings [29]: for MNIST, we generate a UMAP embedding using default hyperparameters, while for the KPMP data we use the UMAP embedding provided with the dataset. For KPMP, we additionally remove mitochondrial and ribosomal genes and use only the top 1000 most variable genes following standard single-cell analysis guidelines [42] (Appendix B.2). We apply LAVA to each dataset, with the neighborhood size hyperparameter  $n$  set to 3000 for MNIST and 500 for KPMP (Appendix A.1). For MNIST, we visualize the correlations of localities or modules as image-sized heatmaps, where the color of each pixel is determined by the sum of its correlations, and additional blue lines are drawn between correlated pixels (visible in most figures; details in Appendix B.4).

### 3.1 Local patterns, global subpatterns

With this experiment, we explore the similarity between correlation patterns across a latent space. **Setup.** We use LAVA locality representations of the MNIST UMAP, without extracted modules. As examples, we select two different localities, and then calculate cosine similarity between their and other localities' respective representations. This is done using correlations for all feature pairs, or using subsets involving only features from the top or bottom half of the images. **Intra- and intercluster heterogeneity.** We observe that patterns of correlations between the original features can be highly dissimilar across localities, even within the same cluster of digits (first column of Figure 3). This can be conceptualized as a multivariate version of Simpson's paradox, wherein different groupings of data – here LAVA localities – can show different trends in association [43], and highlights the fact that local feature associations cannot be trivially summarized across an entire dataset. **Subpatterns of correlations alter similarity.** Considering only locality correlations between pixels from the top or bottom half of the images, we observe variations in the cosine similarities across localities (second and third columns of Figure 3). This indicates how different localities across the latent space might share specific subpatterns of correlation, but not others, which is precisely what the module extraction in LAVA aims to capture.

### 3.2 Module extraction quality and module properties

We analyze the quality of module extraction and the properties of LAVA modules for both datasets.

---

<sup>1</sup>Kidney Precision Medicine Project: <https://www.kpmp.org/>.

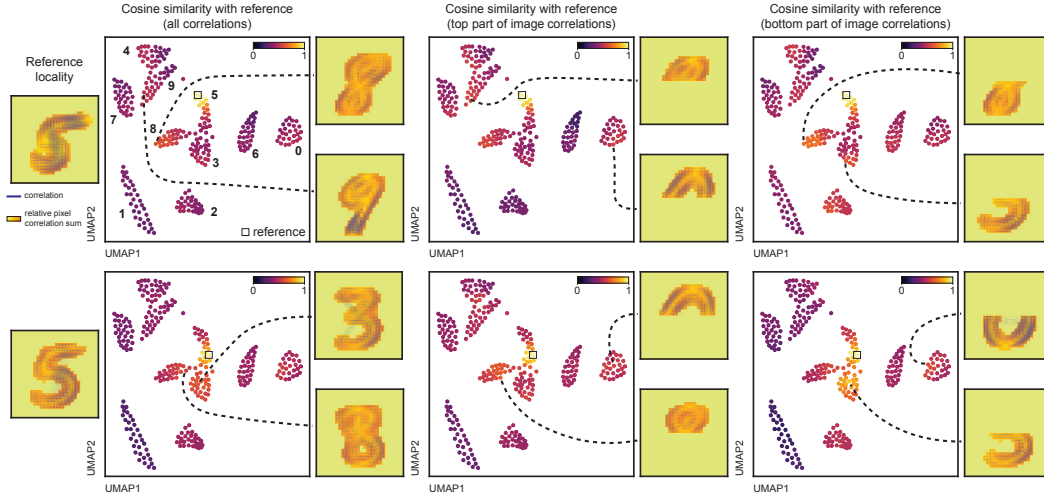


Figure 3: Cosine similarities between each of two reference localities and all other localities of the latent MNIST UMAP space in three settings, with example visualizations of similar localities.

**Setup.** We run module extraction  $R = 10$  times with different numbers of modules  $M$  for each dataset, reporting the main loss term (as cosine similarity instead of distance), overestimation ratio, and silhouette width score (Figure 4). Means and standard deviations of the loss and overestimation ratio are calculated based on the 10 runs. **Stability and reconstruction across runs.** As expected, the loss term cosine similarity increases with larger numbers of modules, resulting in better reconstruction of the original correlations. For MNIST, we observe relatively low silhouette widths irrespective of the number of modules [44], and smaller standard deviations of the loss, pointing to successful optimization and thus a larger number of equally valid solutions. We hypothesize this is due to a large number of common correlation subpatterns, resulting in more ways to reconstruct locality correlations. For KPMP, we see a gradual decrease in stability (silhouette) with larger numbers of modules, indicating more stable solutions for smaller numbers, but similar instability with larger numbers. **Number of modules.** We decided to use 9 modules for both datasets based on the criteria outlined in Subsection 2.3.3. Out of the 10 runs, we chose the one with the lowest loss.

**Modules reveal global subpatterns.** For both datasets, the extracted modules represent globally reoccurring subpatterns not tied to neighboring localities (Figure 5). For MNIST, the first two modules (ordered by sum of presence in the latent space) capture common patterns of correlations between digits 3, 5, and 8, and between digits 4, 7, and 9 (Figure 5a). Visualizations of the two modules also show how the extracted correlations come from pixels shared across the digits these localities represent, as we would expect. We observe similar trends for KPMP embeddings (Figure 5b), with some modules present across most major cell types (module 3), and others pertaining to more local regions of embeddings of more specific cell types (epithelial cells in the case of modules 1, 2, and 4). The module extraction in LAVA uses no information about the spatial organization of localities, allowing it to identify shared subpatterns across clusters, and differentiate patterns within clusters.

**Modules identify reoccurring, not averaged subpatterns.** We observe that AMF extracts modules with overestimation error ratios of around 10% or slightly higher (Figure 4). Errors made up of predominantly underestimation indicate that averaged patterns are avoided in favor of sparser, but actually present subpatterns, which can be seen as a type of quantile regression [37]. Combined with the semantics of cosine similarity, the presence of a module in two localities implies not only a similar subpattern of correlations, but also that the subpattern can directly be observed in both localities.

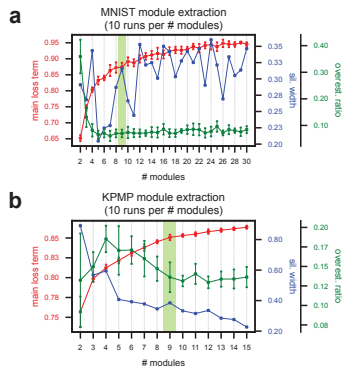


Figure 4: Module extraction results for MNIST and KPMP.

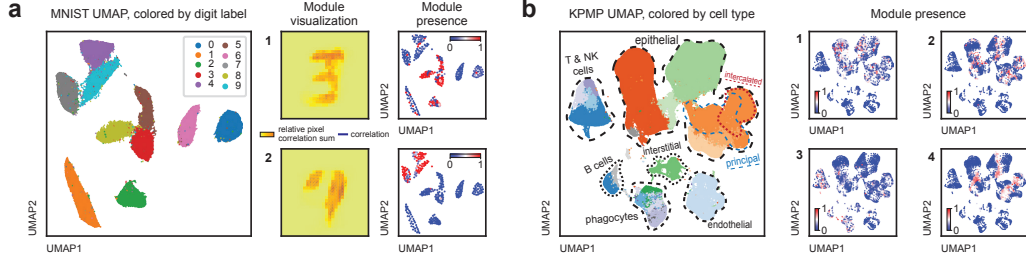


Figure 5: Labels and example module presences for the MNIST and KPMP UMAP embeddings.

We visualize this for MNIST by comparing two extracted modules to what they would look like if their LAVA extracted correlations were replaced by the presence-weighted average across localities. **Multiple modules can coexist in a single locality.** To investigate if LAVA modules can be co-present in the same locality, we scale the presences for each locality to sum to 1, and calculate Shannon entropy to quantify module co-presence per locality in each dataset. Ignoring localities with summed presences  $< 0.5$  to prevent inflated entropies from scaling, we get average values of  $0.68 (\pm 0.41)$  and  $1.41 (\pm 0.75)$  for MNIST and KPMP, respectively (Figures 7a and 7b). For reference, 0 means no overlap between modules and 3.17 corresponds to all 9 modules being equally present. The obtained entropies indicate some overlap in both datasets, more so in KPMP. Figure 7c shows an example of how modules overlap to reconstruct correlations of a locality in MNIST. Allowing overlap, a given locality can be related to different subsets of localities through presences of modules, even when those modules represent partially overlapping subpatterns of correlation.

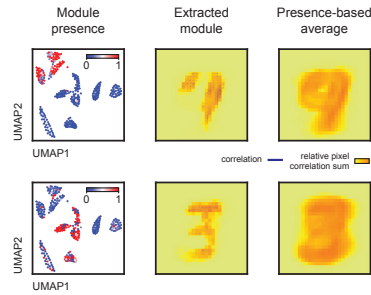


Figure 6: Extracted modules vs. presence-weighted averages.

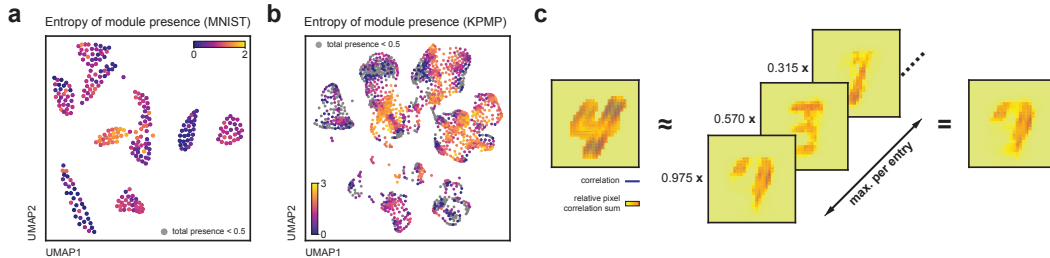


Figure 7: Entropy of module presences per locality for the MNIST and KPMP datasets, with an MNIST example of how modules are combined to reconstruct localities.

### 3.3 Explaining embeddings of gene expression data (KPMP)

We investigate if LAVA modules can reveal biologically relevant patterns using the UMAP of KPMP data. **Setup.** The KPMP dataset includes metadata about the human donors of the cells: we look at disease state, which is either healthy, acute kidney failure (ACF), or chronic kidney disease (CKD). We first calculate percentages of samples from donor disease state per locality. We then calculate Pearson correlations and respective p-values between module presences and these percentages (ignoring localities where a module is not present) to gauge the association between module and disease state. We further investigate if genes in those modules are related to biological pathways related to diseased state (Appendix B.6). **Module correlates with diseased samples.** Cells from patients with different disease states are spread throughout the latent space, with no apparent clustering. However, the presence of module 4 (Figure 5b) is positively correlated with the percentage of diseased samples ( $0.23, p < 0.01$ ), and of CKD samples specifically ( $0.28, p < 0.01$ ). Together with the fact that module 4 is present across epithelial cells and not blood cells, this suggests that the correlation

subpattern of module 4 could be biologically relevant for kidney disease related pathways. **Module genes and disease related pathways.** Overrepresentation analysis of biological pathways [45] for the set of genes in module 4 correlations exhibit 21 significant pathways ( $p < 0.01$ ). To highlight biological relevance, we single out the more general “cellular response to stress” and the DNA damage response pathways, linked to CKD in previous studies [46–49]. Overall, our findings suggest that the local organization of KPMP latent UMAP embeddings across kidney tissue cell types exhibits patterns of gene correlation related to kidney disease. This local structure of sample organization is not apparent in the clustering of the data, but notably discoverable through the LAVA modules.

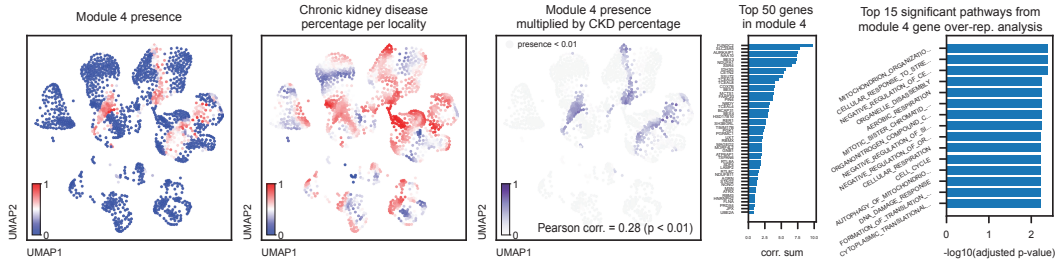


Figure 8: Module 4 for KPMP: overlap with chronic kidney disease and gene analysis.

## 4 Limitations

**Defining neighborhood size.** A larger limitation of LAVA is the definition of a relevant size for localities. Explanations based on local sample groupings are relevant for embeddings produced by techniques like non-linear manifold learning, which themselves try to preserve local relationships, but the choice of neighborhood size remains a challenge. The issue of defining meaningful localities relates more broadly to that of latent axes not corresponding to known quantities or concepts. While in unsupervised settings, exploration of multiple sizes might be of interest, in supervised settings or using metadata, size of locality could be motivated by changes in a target of interest. **Association as correlation, and directionality.** We estimate pairwise association between original features with Spearman correlations, therefore more complex associations will not be captured. Furthermore, our module extraction assumes absolute values, and cannot be trivially extended to differentiate between negative and positive correlation because of its use of the maximum function. This means LAVA cannot differentiate correlation reversals. **Module extraction.** As we saw in MNIST experiments, module extraction can lead to multiple equally good solutions. Assuming the problem setting is well-defined, each of these solutions is worth exploring, which might not always be practically feasible. We did not look into whether some modules are consistent across the different runs, which might be an exploitable finding. Choosing the number of modules used based on a stability/accuracy trade-off also retains some ambiguity, but is inherent to the unsupervised setting. **Unstructured data.** While we experiment with MNIST, our approach is generally suitable for tabular, as opposed to unstructured data such as images and text. With larger adaptations, a concept-based approach looking at presences of concepts rather than correlations between individual features, might be applicable [50].

## 5 Conclusions

In this work, we framed the problem of latent space explainability as enabling reasoning about the relative spatial organization of embeddings and their original data. We focused on explainability for latent embeddings generated by manifold learning that only produce embeddings and no mapping function. To that effect, we introduced the LAVA method, which describes local groups of data in the latent space through observed correlations between features in the original data, and relates them globally to one another by revealing reoccurring subpatterns of correlation throughout the latent space. In future work, we envision further exploring the idea of reasoning about latent embeddings spatially, especially for higher-dimensional latent spaces and supervised tasks, in which the spatial relations between embedded samples can be put into context, and differentiated from one another based on specific targets of interest, which we anticipate to be possible building on top of existing feature and sample importance methods. We see this approach having potential to extract more insight from ML models than existing methods, further aiding in model development and knowledge discovery.

## Acknowledgments and Disclosure of Funding

### The authors.

Authors received funding from the US National Institutes of Health [grant numbers U54EY032442, U54DK134302, U01CA294527, and R01AI138581 to JPG; grant numbers U01DK133766 and R01AG078803 to IS and JPG]. Funders were not involved in the research, authors are solely responsible for this work.

### The KPMP dataset.

The results here are in whole or part based upon data generated by the Kidney Precision Medicine Project. Accessed March 1, 2025. <https://www.kpmp.org>.

Funded by the National Institute of Diabetes and Digestive and Kidney Diseases (Grant numbers: U01DK133081, U01DK133091, U01DK133092, U01DK133093, U01DK133095, U01DK133097, U01DK114866, U01DK114908, U01DK133090, U01DK133113, U01DK133766, U01DK133768, U01DK114907, U01DK114920, U01DK114923, U01DK114933, U24DK114886, UH3DK114926, UH3DK114861, UH3DK114915, UH3DK114937)

## References

- [1] Bas C. Van Fraassen. “The Pragmatic Theory of Explanation”. In: *Theories of explanation*. Ed. by Joseph C. Pitt. Oxford University Press, 1988.
- [2] John Jumper et al. “Highly accurate protein structure prediction with AlphaFold”. In: *Nature* 596.7873 (Aug. 2021). Publisher: Nature Publishing Group, pp. 583–589. ISSN: 1476-4687. DOI: 10.1038/s41586-021-03819-2. URL: <https://www.nature.com/articles/s41586-021-03819-2> (visited on 10/27/2024).
- [3] Alex Davies et al. “Advancing mathematics by guiding human intuition with AI”. In: *Nature* 600.7887 (Dec. 2021). Publisher: Nature Publishing Group, pp. 70–74. ISSN: 1476-4687. DOI: 10.1038/s41586-021-04086-x. URL: <https://www.nature.com/articles/s41586-021-04086-x> (visited on 10/27/2024).
- [4] Rajiv Movva et al. “Deciphering regulatory DNA sequences and noncoding genetic variants using neural network models of massively parallel reporter assays”. In: *PLOS ONE* 14.6 (June 17, 2019). Publisher: Public Library of Science, e0218073. ISSN: 1932-6203. DOI: 10.1371/journal.pone.0218073. URL: <https://journals.plos.org/plosone/article?id=10.1371/journal.pone.0218073> (visited on 10/27/2024).
- [5] Travers Ching et al. “Opportunities and obstacles for deep learning in biology and medicine”. In: *Journal of The Royal Society Interface* 15.141 (Apr. 4, 2018). Publisher: Royal Society, p. 20170387. DOI: 10.1098/rsif.2017.0387. URL: <https://royalsocietypublishing.org/doi/full/10.1098/rsif.2017.0387> (visited on 10/27/2024).
- [6] Zachary C. Lipton. *The Mythos of Model Interpretability*. Mar. 6, 2017. DOI: 10.48550/arXiv.1606.03490. arXiv: 1606.03490[cs]. URL: <http://arxiv.org/abs/1606.03490> (visited on 03/27/2025).
- [7] Paul Humphreys. “The Philosophical Novelty of Computer Simulation Methods”. In: *Synthese* 169.3 (2009). Publisher: Springer, pp. 615–626. DOI: 10.1007/s11229-008-9435-2.
- [8] Claus Beisbart and Tim R az. “Philosophy of science at sea: Clarifying the interpretability of machine learning”. In: *Philosophy Compass* 17.6 (2022), e12830. ISSN: 1747-9991. DOI: 10.1111/phc3.12830. URL: <https://onlinelibrary.wiley.com/doi/abs/10.1111/phc3.12830> (visited on 01/28/2025).
- [9] Cynthia Rudin. “Stop explaining black box machine learning models for high stakes decisions and use interpretable models instead”. In: *Nature Machine Intelligence* 1.5 (May 2019). Publisher: Nature Publishing Group, pp. 206–215. ISSN: 2522-5839. DOI: 10.1038/s42256-019-0048-x. URL: <https://www.nature.com/articles/s42256-019-0048-x> (visited on 10/22/2024).

- [10] W. James Murdoch et al. “Definitions, methods, and applications in interpretable machine learning”. In: *Proceedings of the National Academy of Sciences* 116.44 (Oct. 29, 2019). Publisher: Proceedings of the National Academy of Sciences, pp. 22071–22080. DOI: 10.1073/pnas.1900654116. URL: <https://www.pnas.org/doi/full/10.1073/pnas.1900654116> (visited on 09/18/2024).
- [11] Hanchen Wang et al. “Scientific discovery in the age of artificial intelligence”. In: *Nature* 620.7972 (Aug. 2023). Publisher: Nature Publishing Group, pp. 47–60. ISSN: 1476-4687. DOI: 10.1038/s41586-023-06221-2. URL: <https://www.nature.com/articles/s41586-023-06221-2> (visited on 10/27/2024).
- [12] Irina Higgins et al. *Towards a Definition of Disentangled Representations*. Dec. 5, 2018. DOI: 10.48550/arXiv.1812.02230. arXiv: 1812.02230. URL: <http://arxiv.org/abs/1812.02230> (visited on 10/23/2024).
- [13] Bernhard Schölkopf. *Causality for Machine Learning*. Dec. 23, 2019. DOI: 10.48550/arXiv.1911.10500. arXiv: 1911.10500. URL: <http://arxiv.org/abs/1911.10500> (visited on 10/27/2024).
- [14] Christoph Molnar. *Interpretable Machine Learning. A Guide for Making Black Box Models Explainable*. 2nd ed. 2022. URL: <https://christophm.github.io/interpretable-ml-book>.
- [15] Tom Brown et al. “Language Models are Few-Shot Learners”. In: *Advances in Neural Information Processing Systems*. Vol. 33. Curran Associates, Inc., 2020, pp. 1877–1901. URL: <https://papers.nips.cc/paper/2020/hash/1457c0d6bfc4967418bfb8ac142f64a-Abstract.html> (visited on 11/05/2024).
- [16] Aditya Ramesh et al. “Zero-Shot Text-to-Image Generation”. In: *Proceedings of the 38th International Conference on Machine Learning*. International Conference on Machine Learning. ISSN: 2640-3498. PMLR, July 1, 2021, pp. 8821–8831. URL: <https://proceedings.mlr.press/v139/ramesh21a.html> (visited on 11/05/2024).
- [17] Stavros Makrodimitis et al. “An in-depth comparison of linear and non-linear joint embedding methods for bulk and single-cell multi-omics”. In: *Briefings in Bioinformatics* 25.1 (Jan. 1, 2024), bbad416. ISSN: 1477-4054. DOI: 10.1093/bib/bbad416. URL: <https://doi.org/10.1093/bib/bbad416> (visited on 10/31/2024).
- [18] Dmitry Kobak and Philipp Berens. “The art of using t-SNE for single-cell transcriptomics”. In: *Nature Communications* 10.1 (Nov. 28, 2019). Publisher: Nature Publishing Group, p. 5416. ISSN: 2041-1723. DOI: 10.1038/s41467-019-13056-x. URL: <https://www.nature.com/articles/s41467-019-13056-x> (visited on 11/10/2024).
- [19] Rishi Bommasani et al. *On the Opportunities and Risks of Foundation Models*. July 12, 2022. DOI: 10.48550/arXiv.2108.07258. arXiv: 2108.07258[cs]. URL: <http://arxiv.org/abs/2108.07258> (visited on 05/04/2025).
- [20] Maria Brbić et al. “Annotation of spatially resolved single-cell data with STELLAR”. In: *Nature Methods* 19.11 (Nov. 2022). Publisher: Nature Publishing Group, pp. 1411–1418. ISSN: 1548-7105. DOI: 10.1038/s41592-022-01651-8. URL: <https://www.nature.com/articles/s41592-022-01651-8> (visited on 11/07/2024).
- [21] Wouter Saelens et al. “A comparison of single-cell trajectory inference methods”. In: *Nature Biotechnology* 37.5 (May 2019). Publisher: Nature Publishing Group, pp. 547–554. ISSN: 1546-1696. DOI: 10.1038/s41587-019-0071-9. URL: <https://www.nature.com/articles/s41587-019-0071-9> (visited on 09/09/2024).
- [22] F. Alexander Wolf et al. “PAGA: graph abstraction reconciles clustering with trajectory inference through a topology preserving map of single cells”. In: *Genome Biology* 20.1 (Mar. 19, 2019), p. 59. ISSN: 1474-760X. DOI: 10.1186/s13059-019-1663-x. URL: <https://doi.org/10.1186/s13059-019-1663-x> (visited on 11/10/2024).
- [23] Doron Haviv et al. “The covariance environment defines cellular niches for spatial inference”. In: *Nature Biotechnology* (Apr. 2, 2024). Publisher: Nature Publishing Group, pp. 1–12. ISSN: 1546-1696. DOI: 10.1038/s41587-024-02193-4. URL: <https://www.nature.com/articles/s41587-024-02193-4> (visited on 11/01/2024).

- [24] Jonathan Crabbé and Mihaela van der Schaar. “Label-Free Explainability for Unsupervised Models”. In: *Proceedings of the 39th International Conference on Machine Learning*. International Conference on Machine Learning. ISSN: 2640-3498. PMLR, June 28, 2022, pp. 4391–4420. URL: <https://proceedings.mlr.press/v162/crabbe22a.html> (visited on 10/20/2024).
- [25] Francesco Locatello et al. *A Sober Look at the Unsupervised Learning of Disentangled Representations and their Evaluation*. Oct. 27, 2020. DOI: 10.48550/arXiv.2010.14766. arXiv: 2010.14766. URL: <http://arxiv.org/abs/2010.14766> (visited on 10/31/2024).
- [26] Kevin P. Murphy. *Probabilistic Machine Learning: An introduction*. MIT Press, 2022. URL: <http://probml.github.io/book1>.
- [27] Marina Meilă and Hanyu Zhang. “Manifold Learning: What, How, and Why”. In: *Annual Review of Statistics and Its Application* 11 (Volume 11, 2024 Apr. 22, 2024). Publisher: Annual Reviews, pp. 393–417. ISSN: 2326-8298, 2326-831X. DOI: 10.1146/annurev-statistics-040522-115238. URL: <https://www.annualreviews.org/content/journals/10.1146/annurev-statistics-040522-115238> (visited on 10/28/2024).
- [28] Laurens van der Maaten and Geoffrey Hinton. “Visualizing Data using t-SNE”. In: *Journal of Machine Learning Research* 9.86 (2008), pp. 2579–2605. ISSN: 1533-7928. URL: <http://jmlr.org/papers/v9/vandermaaten08a.html> (visited on 11/05/2024).
- [29] Leland McInnes, John Healy, and James Melville. *UMAP: Uniform Manifold Approximation and Projection for Dimension Reduction*. Sept. 18, 2020. DOI: 10.48550/arXiv.1802.03426. arXiv: 1802.03426. URL: <http://arxiv.org/abs/1802.03426> (visited on 11/05/2024).
- [30] Henry Han et al. “Enhance explainability of manifold learning”. In: *Neurocomputing* 500 (Aug. 21, 2022), pp. 877–895. ISSN: 0925-2312. DOI: 10.1016/j.neucom.2022.05.119. URL: <https://www.sciencedirect.com/science/article/pii/S0925231222007044> (visited on 10/20/2024).
- [31] Etienne Becht et al. “Dimensionality reduction for visualizing single-cell data using UMAP”. In: *Nature Biotechnology* 37.1 (Jan. 2019). Publisher: Nature Publishing Group, pp. 38–44. ISSN: 1546-1696. DOI: 10.1038/nbt.4314. URL: <https://www.nature.com/articles/nbt.4314> (visited on 11/10/2024).
- [32] Yingfan Wang et al. *Understanding How Dimension Reduction Tools Work: An Empirical Approach to Deciphering t-SNE, UMAP, TriMAP, and PaCMAP for Data Visualization*. Aug. 24, 2021. DOI: 10.48550/arXiv.2012.04456. arXiv: 2012.04456. URL: <http://arxiv.org/abs/2012.04456> (visited on 11/09/2024).
- [33] Lucy Xia, Christy Lee, and Jingyi Jessica Li. “Statistical method scDEED for detecting dubious 2D single-cell embeddings and optimizing t-SNE and UMAP hyperparameters”. In: *Nature Communications* 15.1 (Feb. 26, 2024). Publisher: Nature Publishing Group, p. 1753. ISSN: 2041-1723. DOI: 10.1038/s41467-024-45891-y. URL: <https://www.nature.com/articles/s41467-024-45891-y> (visited on 11/10/2024).
- [34] Yang Liu et al. “Latent Space Cartography: Visual Analysis of Vector Space Embeddings”. In: *Computer Graphics Forum* 38.3 (2019). \_eprint: <https://onlinelibrary.wiley.com/doi/pdf/10.1111/cgf.13672>, pp. 67–78. ISSN: 1467-8659. DOI: 10.1111/cgf.13672. URL: <https://onlinelibrary.wiley.com/doi/abs/10.1111/cgf.13672> (visited on 10/26/2024).
- [35] J. MacQueen. “Some methods for classification and analysis of multivariate observations”. In: *Proceedings of the Fifth Berkeley Symposium on Mathematical Statistics and Probability, Volume 1: Statistics*. Vol. 5.1. University of California Press, Jan. 1, 1967, pp. 281–298. URL: <https://projecteuclid.org/ebooks/berkeley-symposium-on-mathematical-statistics-and-probability/Proceedings-of-the-Fifth-Berkeley-Symposium-on-Mathematical-Statistics-and/chapter/Some-methods-for-classification-and-analysis-of-multivariate-observations/bsmsp/1200512992> (visited on 11/09/2024).
- [36] D. R. Jones, C. D. Perttunen, and B. E. Stuckman. “Lipschitzian optimization without the Lipschitz constant”. In: *Journal of Optimization Theory and Applications* 79.1 (Oct. 1, 1993), pp. 157–181. ISSN: 1573-2878. DOI: 10.1007/BF00941892. URL: <https://doi.org/10.1007/BF00941892> (visited on 10/28/2024).

- [37] Roger Koenker and Kevin F. Hallock. “Quantile Regression”. In: *Journal of Economic Perspectives* 15.4 (Dec. 2001), pp. 143–156. ISSN: 0895-3309. DOI: 10.1257/jep.15.4.143. URL: <https://www.aeaweb.org/articles?id=10.1257/jep.15.4.143> (visited on 05/06/2025).
- [38] Ludmil B. Alexandrov et al. “Deciphering Signatures of Mutational Processes Operative in Human Cancer”. In: *Cell Reports* 3.1 (Jan. 31, 2013). Publisher: Elsevier, pp. 246–259. ISSN: 2211-1247. DOI: 10.1016/j.celrep.2012.12.008. URL: [https://www.cell.com/cell-reports/abstract/S2211-1247\(12\)00433-0](https://www.cell.com/cell-reports/abstract/S2211-1247(12)00433-0) (visited on 11/10/2024).
- [39] Y. Lecun et al. “Gradient-based learning applied to document recognition”. In: *Proceedings of the IEEE* 86.11 (Nov. 1998). Conference Name: Proceedings of the IEEE, pp. 2278–2324. ISSN: 1558-2256. DOI: 10.1109/5.726791. URL: <https://ieeexplore.ieee.org/document/726791> (visited on 10/28/2024).
- [40] Blue B. Lake et al. “An atlas of healthy and injured cell states and niches in the human kidney”. In: *Nature* 619.7970 (July 2023). Publisher: Nature Publishing Group, pp. 585–594. ISSN: 1476-4687. DOI: 10.1038/s41586-023-05769-3. URL: <https://www.nature.com/articles/s41586-023-05769-3> (visited on 11/09/2024).
- [41] Rory Stark, Marta Grzelak, and James Hadfield. “RNA sequencing: the teenage years”. In: *Nature Reviews Genetics* 20.11 (Nov. 2019). Publisher: Nature Publishing Group, pp. 631–656. ISSN: 1471-0064. DOI: 10.1038/s41576-019-0150-2. URL: <https://www.nature.com/articles/s41576-019-0150-2> (visited on 05/12/2025).
- [42] Lukas Heumos et al. “Best practices for single-cell analysis across modalities”. In: *Nature Reviews Genetics* 24.8 (Aug. 2023). Publisher: Nature Publishing Group, pp. 550–572. ISSN: 1471-0064. DOI: 10.1038/s41576-023-00586-w. URL: <https://www.nature.com/articles/s41576-023-00586-w> (visited on 05/12/2025).
- [43] Myra L. Samuels. “Simpson’s Paradox and Related Phenomena”. In: *Journal of the American Statistical Association* 88.421 (Mar. 1, 1993). Publisher: ASA Website\_eprint: <https://doi.org/10.1080/01621459.1993.10594297>, pp. 81–88. ISSN: 0162-1459. DOI: 10.1080/01621459.1993.10594297. URL: <https://doi.org/10.1080/01621459.1993.10594297> (visited on 05/11/2025).
- [44] Peter J. Rousseeuw. “Silhouettes: A graphical aid to the interpretation and validation of cluster analysis”. In: *Journal of Computational and Applied Mathematics* 20 (Nov. 1, 1987), pp. 53–65. ISSN: 0377-0427. DOI: 10.1016/0377-0427(87)90125-7. URL: <https://www.sciencedirect.com/science/article/pii/0377042787901257> (visited on 11/11/2024).
- [45] Zhuoqing Fang, Xinyuan Liu, and Gary Peltz. “GSEApY: a comprehensive package for performing gene set enrichment analysis in Python”. In: *Bioinformatics* 39.1 (Nov. 2022), btac757. ISSN: 1367-4811. DOI: 10.1093/bioinformatics/btac757. eprint: <https://academic.oup.com/bioinformatics/article-pdf/39/1/btac757/48448971/btac757.pdf>. URL: <https://doi.org/10.1093/bioinformatics/btac757>.
- [46] Francesco Patera et al. “Kidney Fibrosis and Oxidative Stress: From Molecular Pathways to New Pharmacological Opportunities”. In: *Biomolecules* 14.1 (Jan. 2024). Number: 1 Publisher: Multidisciplinary Digital Publishing Institute, p. 137. ISSN: 2218-273X. DOI: 10.3390/biom14010137. URL: <https://www.mdpi.com/2218-273X/14/1/137> (visited on 05/14/2025).
- [47] Nicole Schupp, Helga Stopper, and August Heidland. “DNA Damage in Chronic Kidney Disease: Evaluation of Clinical Biomarkers”. In: *Oxidative Medicine and Cellular Longevity* 2016.1 (Jan. 2016). Publisher: John Wiley & Sons, Ltd, p. 3592042. ISSN: 1942-0900. DOI: 10.1155/2016/3592042. URL: <https://onlinelibrary.wiley.com/doi/10.1155/2016/3592042> (visited on 05/14/2025).
- [48] Bruce A. Molitoris. “DNA damage response protects against progressive kidney disease”. In: *The Journal of Clinical Investigation* 129.11 (), pp. 4574–4575. ISSN: 0021-9738. DOI: 10.1172/JCI131171. URL: <https://www.ncbi.nlm.nih.gov/pmc/articles/PMC6819138/> (visited on 05/14/2025).
- [49] Peipei Wang et al. “Roles of DNA damage in renal tubular epithelial cells injury”. In: *Frontiers in Physiology* 14 (Apr. 6, 2023), p. 1162546. ISSN: 1664-042X. DOI: 10.3389/fphys.2023.1162546. URL: <https://www.ncbi.nlm.nih.gov/pmc/articles/PMC10117683/> (visited on 05/14/2025).

- [50] Jonathan Crabbé and Mihaela van der Schaar. “Concept activation regions: a generalized framework for concept-based explanations”. In: *Proceedings of the 36th International Conference on Neural Information Processing Systems*. NIPS '22. Red Hook, NY, USA: Curran Associates Inc., Nov. 28, 2022, pp. 2590–2607. ISBN: 978-1-7138-7108-8. (Visited on 05/11/2025).
- [51] Richard Connor. “A Tale of Four Metrics”. In: *Similarity Search and Applications*. Ed. by Laurent Amsaleg, Michael E. Houle, and Erich Schubert. Cham: Springer International Publishing, 2016, pp. 210–217. ISBN: 978-3-319-46759-7. DOI: 10.1007/978-3-319-46759-7\_16.
- [52] Ingo Steinwart and Andreas Christmann. “Estimating conditional quantiles with the help of the pinball loss”. In: *Bernoulli* 17.1 (Feb. 2011). Publisher: Bernoulli Society for Mathematical Statistics and Probability, pp. 211–225. ISSN: 1350-7265. DOI: 10.3150/10-BEJ267. URL: <https://projecteuclid.org/journals/bernoulli/volume-17/issue-1/Estimating-conditional-quantiles-with-the-help-of-the-pinball-loss/10.3150/10-BEJ267.full> (visited on 05/21/2025).
- [53] Diederik P. Kingma and Jimmy Ba. *Adam: A Method for Stochastic Optimization*. Jan. 30, 2017. DOI: 10.48550/arXiv.1412.6980. arXiv: 1412.6980. URL: <http://arxiv.org/abs/1412.6980> (visited on 11/10/2024).
- [54] Da Wei Huang, Brad T. Sherman, and Richard A. Lempicki. “Bioinformatics enrichment tools: paths toward the comprehensive functional analysis of large gene lists”. In: *Nucleic Acids Research* 37.1 (Jan. 1, 2009), pp. 1–13. ISSN: 0305-1048. DOI: 10.1093/nar/gkn923. URL: <https://doi.org/10.1093/nar/gkn923> (visited on 05/21/2025).

## A Methodology

### A.1 Locality Definition

#### A.1.1 Hyperparameter $n$ : size of locality

The choice of  $n$  is important as the definition of localities has a substantial influence on correlations that LAVA will calculate in the step (2), and subsequently on module extraction in step (3). A data-driven way of choosing the value  $n$  can be looking at which size of latent neighborhood most resembles the neighborhoods in the original feature size. In choosing such a  $n$ , we attempt to capture localities at a scale that most accurately represents organization in the original feature space. Another, more targeted, approach is motivating the choice of  $n$  using metadata of interest. This might ground the scale of localities to existing knowledge and make findings more relevant for a downstream task. We employ both approaches in our experiments in Section 3, and deliberate further in B.3.

#### A.1.2 Defining the number of localities

To determine the number of localities (and respective probes),  $\ell$ , we look at three factors: the number of embeddings  $E$ , the size of the neighborhood  $n$ , and an additional hyperparameter  $o$  relating to the overlap between localities.  $\ell$  is then defined as:

$$\ell = \lceil E * o/n \rceil, \tag{8}$$

where  $\lceil \cdot \rceil$  denotes rounding to the nearest integer. The hyperparameter  $o$  determines the number of localities given a dataset and neighborhood size  $n$ . If all samples were of a similar centrality (e.g., if data are uniformly spread in some space),  $o = x$  would mean that each sample would be represented by approximately  $x$  localities. A larger  $o$  will produce more overlap between localities and enable a representation that more closely approximates the samples’ original in-degree centralities, but will be more expensive computationally and harder to manage in subsequent analysis. We recommend using smaller values of  $o$  in the range of 2 to 20, so that the resulting number of localities  $\ell$  is manageable, but still captures the various correlation patterns and how they change across the latent space.

#### A.1.3 Optimizing locality placement

For locality placement, we try to match the relative in-degree centralities of samples when we look at the neighborhoods of all samples and the neighborhoods of localities (see Section 2 and Equation 2). We do this by optimizing parameters  $\alpha$  and  $\beta$  from Equation 2 using the  $k$ -means (here referred to as  $\ell$ -means) and DIRECT algorithms [36]. We use Manhattan instead of Euclidean distances to focus less on outliers and approximate centrality more equally across the samples (conceptually, this is similar to the difference between using mean absolute and mean squared errors). The rationale for using the weighing scheme in Equation 1 is forcing the computationally cheap  $\ell$ -means algorithm to optimize locality placement so that Equation 2 is minimized. We want to weigh samples based on their centrality, since the  $\ell$ -means algorithm optimizes Euclidean distances rather than our objective. Furthermore, the weights in Equation 1 factor in the inverse average distances to offset the fact that  $\ell$ -means optimizes the sum of squared Euclidean distances between points, which means that lower density regions of the latent space would have more probes (and localities), even when we weigh samples according to their centrality. Put together: we let the DIRECT algorithm optimize the weights of samples for the  $\ell$ -means algorithm, such that the localities produced by the  $\ell$ -means algorithm minimize our centrality-based loss function. Note that we use only the resulting centroids of the optimization as probes, while cluster assignments produced by the  $\ell$ -means algorithm are ignored. The  $\ell$  localities are then simply the  $n$ -sized neighborhoods around each of the  $\ell$  probes.

Additionally, the DIRECT algorithm requires a range of values for the parameters in which the loss function is convex. We fix this to  $[-4, 4]$  for both  $\alpha$  and  $\beta$ . We conjecture that, at least approximately (especially since  $\ell$ -means is stochastic), the loss function is convex in that interval and contains a good solution. Loosely, as mentioned above, we want the weighing scheme to be able to overpower the overrepresentation of low-density regions that might occur if we would simply weigh samples based on their centrality. We argue about it in terms of hyperball volume: the hyperball volume is proportional to the  $D_L$ -th power of its radius, which for a neighborhood of a sample we can approximate by the average distance to its neighbors, where  $D_L$  is the dimensionality of the latent space. To battle overrepresentation, we then want to weigh samples with larges “volumes” (samples

in low density regions) inversely to their volume, so as to effectively force  $\ell$ -means to give them less importance than they might otherwise have given the squared Euclidean distance optimization. In the two-dimensional case, the hyperball volume is simply the area of the circle, which is proportional to the square of the radius (the average distance of the  $n$  nearest neighbors). To allow weighing in such a fashion, we allow  $\alpha$  to be at least 2, and we further multiply by 2 to allow for exaggeration of this principle. Since we cannot be sure how this weighing will interact with centrality weighing, we allow both parameters to also be negative, and give them the same range, arbitrarily. In our limited experimentation, and with no ground truth to compare to, this seemed to yield good and intuitive results (Figures S5 and S11). If we were to use a higher-dimensional latent space, we would set the range to  $[-2D_L, 2D_L]$ .

The pseudocode, omitting details about DIRECT, is shown in Algorithm S1. We use the `scipy`<sup>1</sup> implementation of the DIRECT algorithm, and the `scikit-learn`<sup>2</sup> implementation of  $k$ -means.

---

**Algorithm S1** Locality placement algorithm.

---

**Require:**  $\mathbf{X} \in \mathbb{R}^{E \times D_L}, \ell$   
**Initialize**  $nearest\_neighbors[E, n], in\_neighborhood[E], avg\_n\_distance[E]$   
 $nearest\_neighbors \leftarrow calculate\_nearest\_neighbors(\mathbf{X}, n)$   
**for**  $i \in \{1, 2, \dots, E\}$  **do**  
     $avg\_n\_distance[i] \leftarrow \frac{1}{n} \sum_{j=1}^n \|\mathbf{X}_i - nearest\_neighbors[i, j]\|_2$   
     $in\_neighborhood[i] \leftarrow \frac{1}{E} \sum_{j=1}^E \mathbb{1}[\mathbf{X}_i \in nearest\_neighbors[j]]$   
**end for**  
  
**Initialize**  $localities[\ell, n], probe\_set[\ell], \alpha_{opt}, \beta_{opt}$   
 $\alpha_{opt}, \beta_{opt} \leftarrow locality\_optimization_{DIRECT}^3(\mathbf{X}, \ell, in\_neighborhood, avg\_n\_distance)$   
 $probe\_set \leftarrow k\_means(\ell, \alpha_{opt}, \beta_{opt}).centroids()$   
 $localities \leftarrow calculate\_nearest\_neighbors(probe\_set, n)$

---

## A.2 Locality Representation

Each locality’s correlations are calculated using the standard formulation of the Spearman correlation:

$$r_s(\mathbf{X}_i, \mathbf{X}_j) = \frac{cov[\mathbf{R}(\mathbf{X}_i), \mathbf{R}(\mathbf{X}_j)]}{\sigma_{\mathbf{R}(\mathbf{X}_i)}, \sigma_{\mathbf{R}(\mathbf{X}_j)}}, \tag{9}$$

where  $X_i$  and  $X_j$  are two original input features and  $\mathbf{R}$  is a ranking function. Covariance  $cov$  and standard deviations  $\sigma$  are estimated from the samples within a locality using standard estimators. Overlapping ranks are averaged.

Importantly, if one of the variables has the same value in 75% of the neighborhood, that correlation is set to 0 for that locality. This is done to prevent overestimation of correlations in cases where there is very little change. Notably, this has been the case for both the MNIST and KPMP datasets in our experiments, as the values of most pixels in MNIST are 0, while gene expression at the single-cell level in KPMP is generally also very sparse. The value of 75% was set arbitrarily, to allow for some leniency, but also avoid meaningless correlations based on low numbers of samples.

## A.3 Module Extraction

### A.3.1 AMF loss function and hyperparameters

The AMF loss function (Equation 6) is discussed in Section 2.3. Here, we provide some additional detail and motivation.

**Different metrics of (dis)similarity.** We decided to use cosine distance for the main term of our loss function. However, a different metric (or divergence) for assessing multivariate (dis)similarity might be equally suitable, e.g., the Kullback-Leibler divergence. Pending further investigation, we did not

---

<sup>1</sup><https://scipy.org/>.

<sup>2</sup><https://scikit-learn.org/>.

<sup>3</sup>More information in Section A.1.3.

assess whether the semantics of one of these might be more appropriate for our task than the other. Some work relating to semantics and efficiency of these metrics suggests triangular distance as a more appropriate choice in most contexts [51].

**Up-weighting overestimation and connection to quantile regression.** The  $\nu$  hyperparameter in Equation 6 determines how up-weighted overestimation errors will be in our loss. Weighing the errors is done similarly to how it is done in univariate quantile regression. The loss for univariate  $\tau$ -th quantile regression, also known as the pinball loss [52], is defined as:

$$\mathcal{L}_\tau(y, f(x)) = \begin{cases} \tau |y - f(x)| & \text{if } y \geq f(x) \\ (1 - \tau) |y - f(x)| & \text{if } y < f(x) \end{cases}. \quad (10)$$

Practically speaking, univariate quantile regression produces a weighing scheme between overestimation and underestimation errors: if  $\tau > 0.5$ , we are less concerned with overestimating  $y$  using  $f(x)$ , and vice versa. Using a  $\tau = 0.5$  is equal to doing median regression, which corresponds to a regression that minimizes the mean absolute error rather than using the more standard mean squared error. For more intuition, we recommend reading [37] and [52].

The idea for module extraction is to retain the semantics of similar, scale-invariant patterns we get with cosine distance or a similar metric, but allowing for reasoning about the reconstructed correlations in terms similar to quantile regression. Retaining the error weighing with a  $\tau < 0.5$  is therefore done to prevent averaging across samples and extract only shared, reoccurring correlations (Section 2.3). Quantile-regression-like reconstructions will allow us to say that correlations present in module-based reconstructions are actually present in the localities with some certainty, or, in terms of errors, that the value of a correlation will be overestimated by at most  $\tau$  (approximately). We can quantify whether this is actually the case by looking at the overestimation errors (Figure 4), which we calculate as the amount of overestimation errors divided by the total absolute error.

Our hyperparameter  $\nu$  that weighs overestimation effectively corresponds to the ratio of weights for the overestimation and underestimation:

$$\nu = \frac{1 - \tau}{\tau}. \quad (11)$$

Using  $\nu$  for weighing overestimation errors when using the mean absolute errors would be equivalent to doing  $\tau$ -th quantile regression. We have set the hyperparameter  $\nu = 9$  in all of our experiments. If we look at the pinball equivalent  $\tau$ , this would correspond to weighing in 0.1-th quantile regression. We cannot make direct parallels since we do not optimize the mean absolute error, but we can observe relative amounts of overestimation, which seem to more-or-less correspond to values we would expect if we would to quantile regression (Figure 4).

**Extra: Presence fine-tuning.** While we do not use it in our experiments, our implementation also includes what we call presence fine-tuning. After selecting modules, we can fix the module matrix  $\mathbf{M}$  and optimize the presence matrix  $\mathbf{P}$  with a pinball loss function (Equation 10), to guarantee that each locality (independent when  $\mathbf{M}$  is fixed) has an overestimation ratio exactly equal to some  $\tau$ . Notice that the modules we find are contingent on the overestimation weighing used in the main loss term, which means that it is not equivalent to first extract, and then simply do fine-tuning at the end.

**Scale regularization.** The second term in Equation 6 is a simple mean absolute error term designed to retain scale of reconstruction. The idea behind scaling is simply to make reconstructions of the same scale as the actual locality correlations, as cosine distance is in itself scale invariant. While the cosine similarity should remain relatively unaffected by this regularization, given a low enough hyperparameter  $\gamma$ , matching scale of the actual locality correlations and our reconstructions will allow us to observe the overestimation ratio of solutions (Section 3; Figure 4). Furthermore, due to scale invariance of cosine distance, it is also imaginable that modules avoid overestimation simply by retaining low correlations values across the board: the scaling should push optimization away from such solutions. It is crucial that the scale regularization contains no overestimation weighing, meaning that the ratio of overestimation is purely a result of the up-weighting in the first term of the loss function. This ensures the retainment of the semantics of reoccurring pattern semantics, rather than focusing on absolute values of our solutions. We set  $\gamma = 0.0001$  as the default value for scale regularization to have a low impact on the loss function. We also end up manually setting this hyperparameter for the KPMP dataset in the experiments (see Section B.3.2), as we noticed  $\gamma = 0.001$  had no effect on optimization because of the low amounts of observed correlation.

**Optimization hyperparameters.** The matrices  $\mathbf{P}$  and  $\mathbf{M}$  are optimized to minimize the loss function (Equation 6) using gradient descent with minibatches of 64 samples (arbitrarily set), the ADAM optimizer [53] with default hyperparameters, and clamping. Clamping is used to force any entries of matrices  $\mathbf{P}$  and  $\mathbf{M}$  to be within the  $[0, 1]$  interval after each step in training. Training is performed until convergence, which we defined as no improvement in the loss function above 1% in 100 epochs. After convergence, we use the matrices from the iteration with the lowest loss as the final solutions. We developed the code based on the PyTorch library<sup>4</sup>.

## B Experiments

### B.1 Software and hardware

All our code was developed using Python 3.8 and its libraries<sup>5</sup>. We ran experiments on Linux compute nodes, comprising of a number of different CPUs and GPUs, details of which we omit to ensure anonymity. Locality placement and correlation calculations took several hours for both datasets. A single module extraction run would take about 5 to 30 minutes, increasing with the number of modules,  $M$ . We also tested all of our code on an Apple M3 Pro with 12 CPU cores and 18GB of RAM, which is what we also used to run Jupyter notebooks for result analysis and plot generation.

### B.2 Datasets, embeddings, and preprocessing

#### B.2.1 MNIST

The MNIST dataset was downloaded using the Scikit-learn Python library<sup>6</sup> library. No preprocessing was performed on the data. Prior to running LAVA, we created a UMAP embedding of the dataset using the UMAP<sup>7</sup> library, with default hyperparameters.

#### B.2.2 KPMP single-cell kidney atlas, v1.5

The KPMP single-cell kidney atlas was downloaded from the CELLxGENE website<sup>8</sup>. The dataset contains a UMAP embedding of the data preprocessed using the Seurat library<sup>9</sup>, which we used for our experiments. More information can be found at the KPMP data portal website<sup>10</sup>. The UMAP of the data can also be explored on the CELLxGENE website<sup>11</sup>. For module extraction, we removed mitochondrial, ribosomal, and mitochondrial ribosome genes. Then, we selected the top 1000 most variable genes, based on the gene expression data (after normalization and log transformation).

### B.3 LAVA hyperparameters

#### B.3.1 Size of locality, $n$

**Data-driven approach (MNIST).** A data-driven way of choosing the value  $n$  can be looking at the Jaccard similarity of neighborhoods of varying sizes in the original space and the latent space. Even though methods such as UMAP have hyperparameters that represent the size of neighborhoods that will be optimized for, different neighborhood sizes might end up being optimized (depending on the choice of other hyperparameters and the dataset). For the UMAP of the MNIST dataset used in our experiments (Section 3), we found that with the default hyperparameter of 15 nearest neighbors, the resulting embedding neighborhoods were most representative of the neighborhoods in the original feature space when  $k \approx 3000$  (Figure S1), which was the value we used for LAVA’s hyperparameter in our experiments with MNIST.

---

<sup>4</sup><https://pytorch.org/>.

<sup>5</sup>Code included with supplementary material and will be made available online, conditional on acceptance.

<sup>6</sup><https://scikit-learn.org>.

<sup>7</sup><https://umap-learn.readthedocs.io>.

<sup>8</sup><https://cellxgene.cziscience.com>. Specific dataset version: <https://datasets.cellxgene.cziscience.com/f5b6d620-76df-45c5-9524-e5631be0e44a.h5ad>.

<sup>9</sup><https://satijalab.org/seurat/>.

<sup>10</sup><https://atlas.kpmp.org/>.

<sup>11</sup><https://cellxgene.cziscience.com/e/dea717d4-7bc0-4e46-950f-fd7e1cc8df7d.cxg/>.

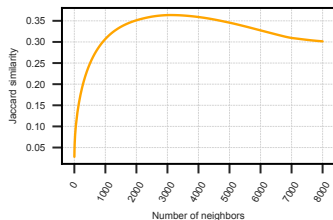


Figure S1: Average Jaccard similarity between original and latent space neighborhoods, calculated for a UMAP of the MNIST dataset with default parameters. Despite the default neighborhood size parameter being 15, we found the highest original neighbor retention to be around 3000 neighbors.

**Meta-data approach (KPMP).** For the KPMP dataset, we were interested in observing patterns of gene correlation on a sub-cell type level. Looking at cell types in the data, we observed the median number of cells for each cell type was 3592, while the smallest cell type had 148 cells (Table S1). Accordingly, we chose neighborhoods of size  $k = 500$ , as this seemed like a large enough number to capture correlations between gene expression that cannot be considered noise, while small enough to explore differences within most of the cell types.

Table S1: Quartile statistics of the numbers of samples per cell type.

	min.	25%	50%	75%	max.
# cells	148	1665	3592	9105	54025

### B.3.2 Module extraction hyperparameters

For module extraction on both MNIST and KPMP, we use default hyperparameters, as defined in Appendix A.3, with one exception: the  $\alpha$  regularization hyperparameter from Equation 6 in KPMP module extraction.  **$\alpha$  for KPMP module extraction.** In our runs, we noticed that using low values for  $\alpha$  resulted in high overestimation error ratios. This pointed to the fact that regularization was mostly likely not affecting the loss function. We assumed this was due to the sparsity of gene expression, and subsequent low correlations in many localities. Running module extraction several times, using higher values of  $\alpha$ , confirmed this hypothesis (Figure S2). Increasing the strength of regularization seemed to have no or negative effect on the quality or stability of solutions (the main loss term and silhouette width, respectively). For our experiments, we ended up using  $\alpha = 10$ , resulting in relatively stable and low error overestimation ratios (Figure S2a).

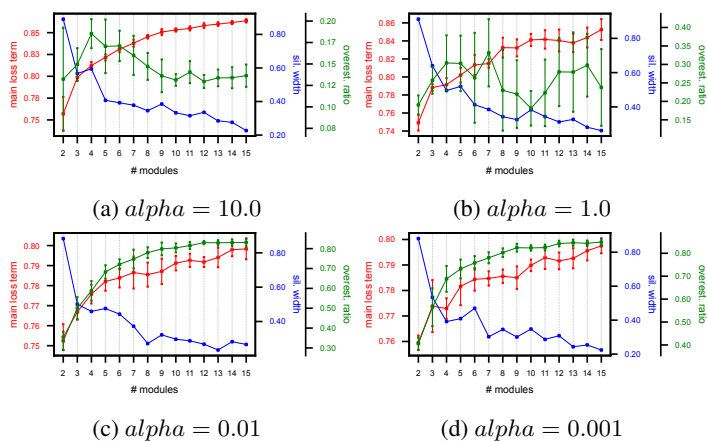


Figure S2: Module extraction runs with different regularization hyperparameter  $\alpha$ .

#### B.4 Visualizations of correlations for the MNIST dataset

The MNIST dataset consists of images that are 28 pixels high and wide, totaling 784 pixels. To show the importance of each feature in a correlation matrix, we create a heatmap of the same dimensionality ( $28 \times 28$ ), where the value of a pixel correspond to the sum of the correlations that pixel participates in. Coloring is relative, meaning that it conveys relative importance of pixels for one locality or module (and its corresponding correlation matrix) only, and not across different visualizations. Furthermore, we add lines to connect pixels that are correlated to one another. This helps visualize the correlations which cause some pixels to be important in the first place. To avoid clutter, we exponentiate correlations to the power of 3, and then remove correlations that are lower than 0.1 after exponentiation (arbitrarily, for visual clarity). The widths of lines that represent correlations are proportional to their exponents to differentiate between stronger and weaker correlations. Some additional examples of visualizations can be seen in Figure S3.

Intuitively, we can think about these visualizations as a way to visualize pixel movement in a group of samples. In the case of local groups of similar images of digits, like we had in our experiments with MNIST, we can ascertain correlations will most likely reflect changes in pixel intensity due to minor translations, rotations, stretchings, or shrinkings of images. Firstly, for all of these transformations, we can expect that nearby pixels will be correlated, which we can see in all visualizations (Figure S3). For the latter three transformations, we can also expect further apart pixels to show patterns of correlation, which we see more clearly in correlations relating to the digits 0 and 1, and in some other localities.

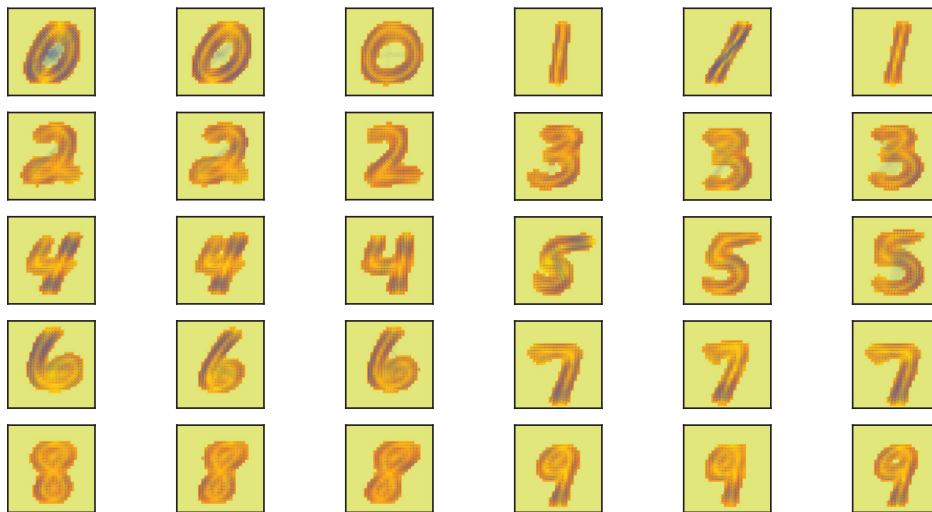


Figure S3: Example visualizations of correlations at various localities from our experiments with the MNIST dataset.

## B.5 MNIST experiments

Here, we show some extra figures and results relating to experiments done with the MNIST dataset. In Figure S4, we show the class labels of individual samples in our UMAP embeddings. Then, in Figure S5, we show the relative in-degree centralities of samples when looking at all the neighborhoods and when looking at our locality placement. In Figure S6, we visualize all modules and their presences used in our experiments from Section 3. We also show modules and presences for the second and third best solutions when  $L = 9$  (Figure S7 and Figure S8). Finally, in Figure S9, we visualize how the chosen modules would look like if they were the presence-weighted average of their localities' correlations, rather than overlapping patterns we extract with AMF (see Section 3).

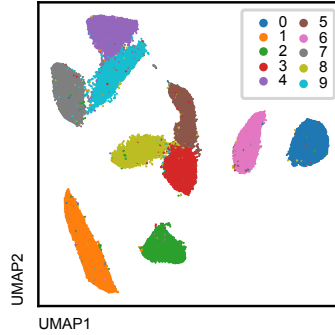
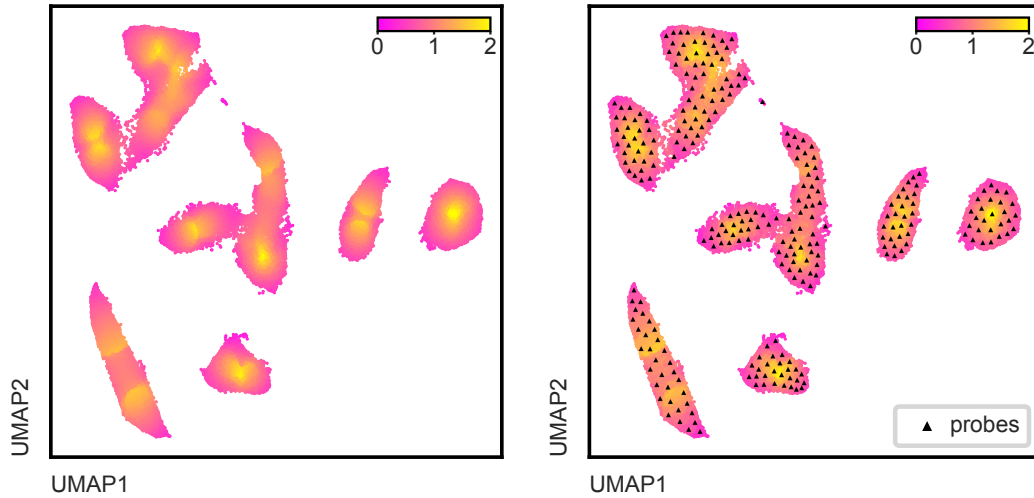


Figure S4: MNIST digit labels across UMAP.



(a) Scaled sample neighborhood in-degree centrality. (b) Scaled locality in-degree centrality, with probes.

Figure S5: MNIST UMAP sample relative centralities before and after locality placement (scaled by  $\frac{E}{k}$  to have an average of 1).

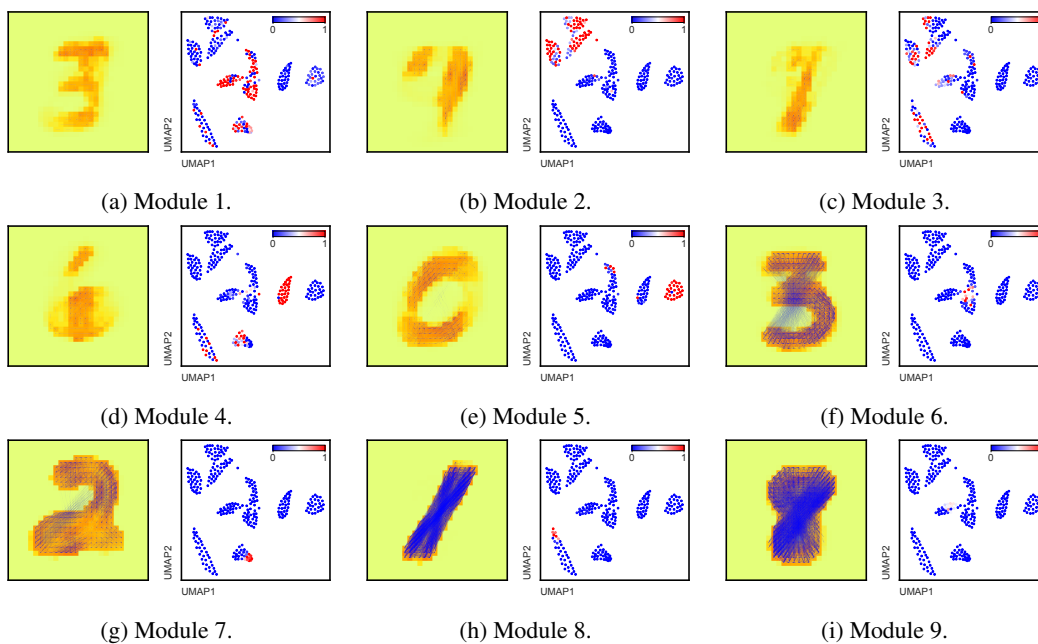


Figure S6: Visualizations and presences of the 9 extracted modules for MNIST.

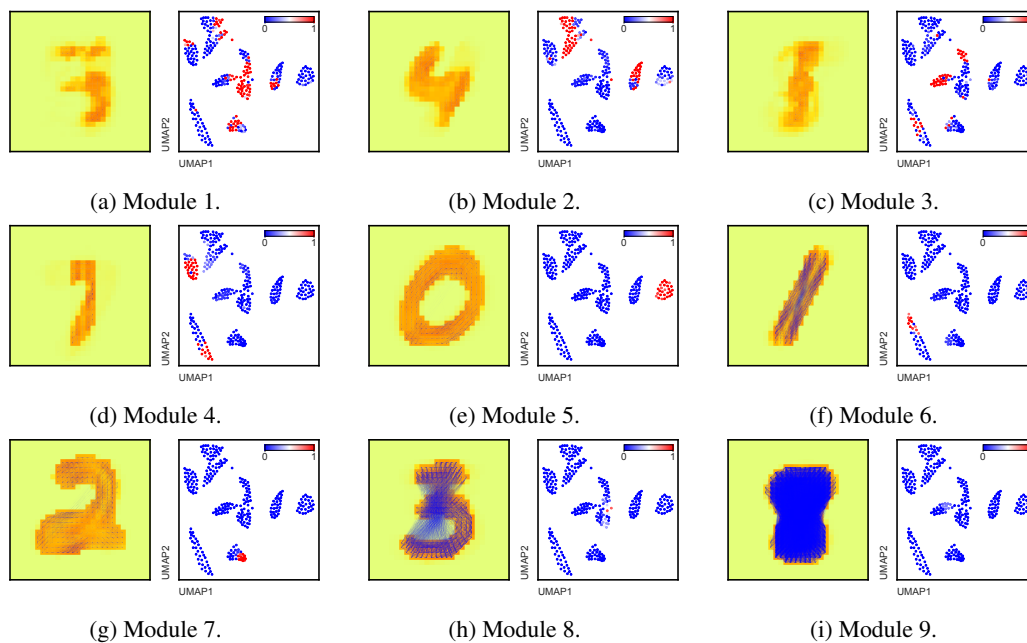


Figure S7: Visualizations and presences of the second best 9 modules for MNIST.

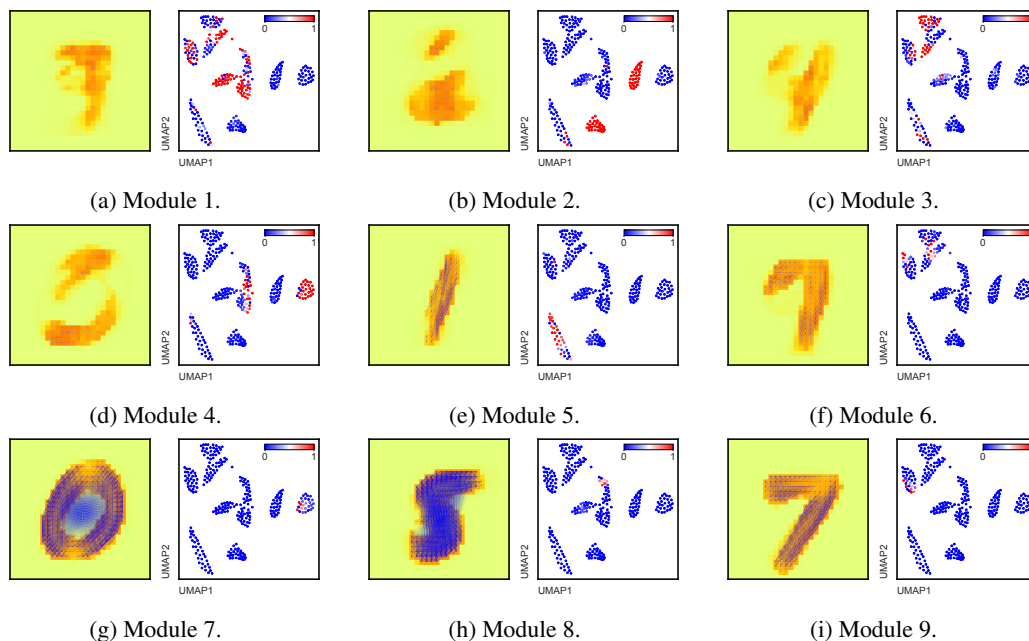


Figure S8: Visualizations and presences of the third best 9 modules for MNIST.

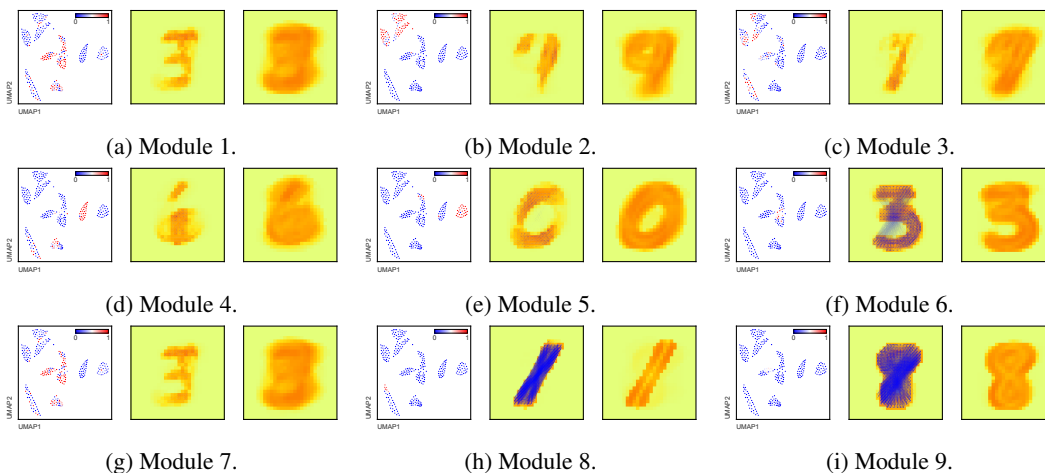


Figure S9: Presences, actual extracted modules, and what modules would look like if they were presence-weighted averages of the localities they reconstruct, for the 9 extracted MNIST modules.

## B.6 KPMP experiments

Here, we show some extra figures and results relating to experiments done with the KPMP dataset, and we provide more details on the gene set analysis done in Section 3.3.

### B.6.1 Additional figures and results.

In Figure S10, we show cell type and disease category labels for all the samples in the UMAP embeddings. In Figure S11, we show the relative in-degree centralities of samples when looking at all the neighborhoods and when looking at our locality placement. In Figure S12, we show the presences of modules chosen for experiments (Section 3.3).



Figure S10: KPMP metadata.

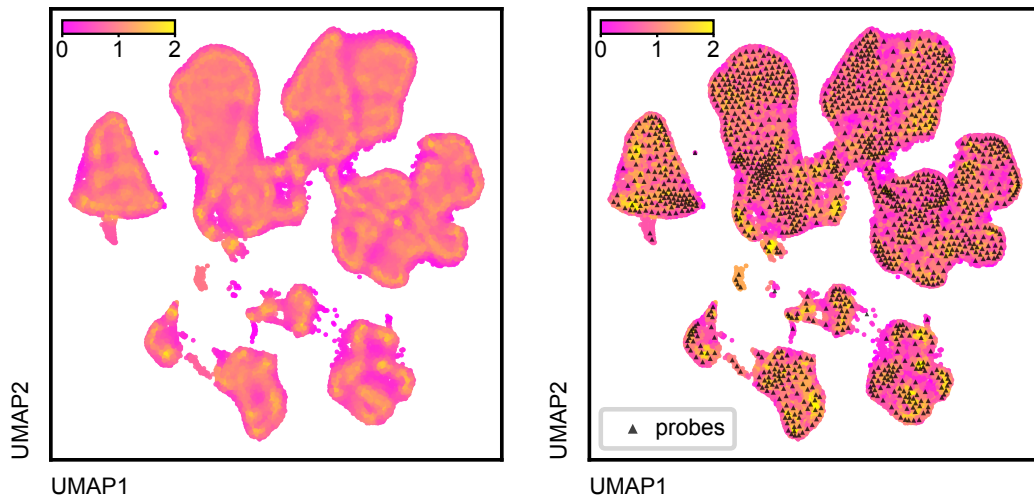


Figure S11: KPMP UMAP relative sample centralities before and after locality placement (scaled by  $\frac{E}{k}$  to have an average of 1).

**Disease category.** In Section 3.3, we analyze our modules in relation to disease category of patients from whom the single-cell samples come from. To get a better sense of the data, in Figure S13, we visualize the ratios of diseased samples across LAVA’s localities. **Correlations between module presences and disease category ratios.** For each of the modules, we also report correlations between the presences of that module and the ratios of the three different disease categories (Table S2). We calculate correlations only across localities in which the module is actually present, that is, with presence  $> 0.01$ . We do this because we do not expect that a pattern of correlations in a locality will be caused purely by the number of disease samples. Therefore, we also do not expect any module

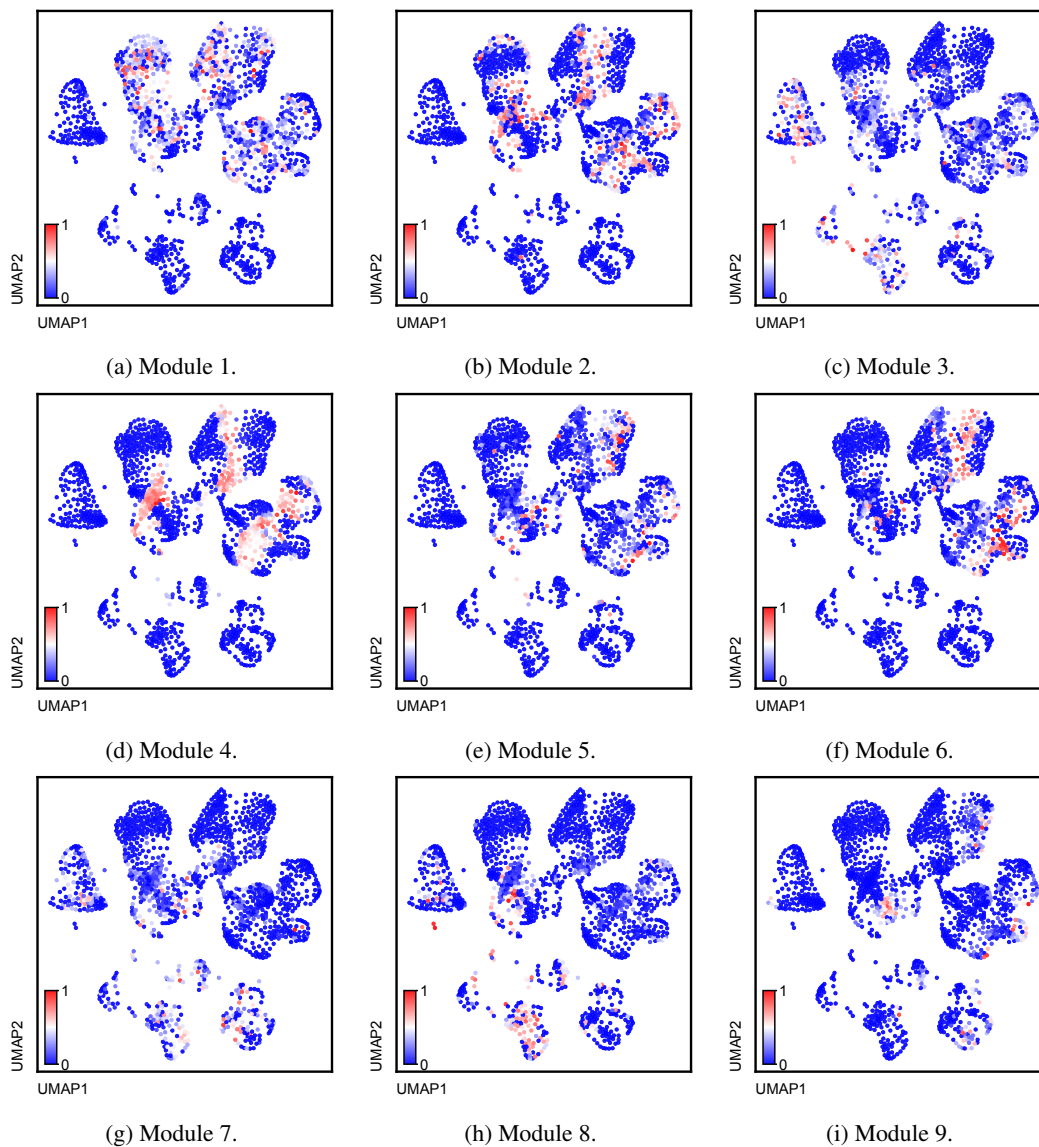


Figure S12: Presences of the 9 extracted modules for KPMP.

presences to directly reflect the number of disease samples across the localities. However, we do expect that the presence of a module might reflect the relative number of disease samples across the localities it is present in, as a disease could have a specific influence on gene expression for specific cells, and hence also the correlations we might observe when looking at the embeddings locally.

	CKD + AKF, Pear.	CKD + AKF, Spear.	CKD, Pear.	CKD, Spear.	AKF, Pear.	AKF, Spear.
m. 1	-.06 ( $p = .116$ )	-.06 ( $p = .139$ )	-.11 ( $p = .005$ )	-.08 ( $p = .035$ )	.07 ( $p = .049$ )	.07 ( $p = .052$ )
m. 2	.01 ( $p = .865$ )	.03 ( $p = .473$ )	-.03 ( $p = .592$ )	-.02 ( $p = .62$ )	.05 ( $p = .292$ )	.08 ( $p = .095$ )
m. 3	-.01 ( $p = .878$ )	-.05 ( $p = .242$ )	-.18 ( $p < .001$ )	-.20 ( $p =$ )	.23 ( $p < .001$ )	.25 ( $p < .001$ )
m. 4	.23 ( $p < .001$ )	.26 ( $p < .001$ )	.28 ( $p < .001$ )	.28 ( $p < .001$ )	-.05 ( $p = .269$ )	.03 ( $p = .501$ )
m. 5	-.05 ( $p = .219$ )	-.08 ( $p = .092$ )	-.11 ( $p = .010$ )	-.14 ( $p = .002$ )	.09 ( $p = .042$ )	.08 ( $p = .065$ )
m. 6	-.08 ( $p = .107$ )	-.07 ( $p = .173$ )	-.13 ( $p = .010$ )	-.13 ( $p = .013$ )	.08 ( $p = .126$ )	.12 ( $p = .014$ )
m. 7	-.31 ( $p < .001$ )	-.36 ( $p < .001$ )	-.28 ( $p < .001$ )	.28 ( $p < .001$ )	-.01 ( $p = .846$ )	-.01 ( $p = .790$ )
m. 8	-.13 ( $p = .008$ )	-.17 ( $p < .001$ )	-.22 ( $p < .001$ )	-.20 ( $p < .001$ )	.14 ( $p = .003$ )	.11 ( $p = .028$ )
m. 9	.10 ( $p = .084$ )	.09 ( $p = .127$ )	.04 ( $p = .429$ )	.06 ( $p = .310$ )	.09 ( $p = .099$ )	.14 ( $p = .015$ )

Table S2: Correlations between module presences and disease categories.

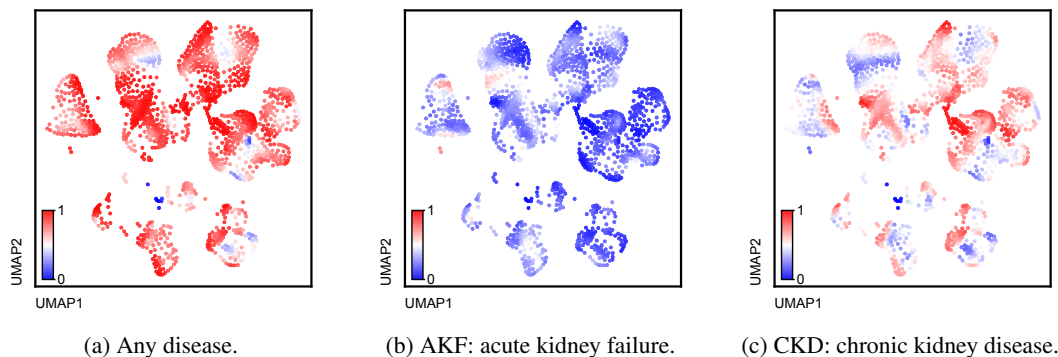


Figure S13: Percentage of disease categories across localities.

### B.6.2 Gene pathway analysis

In Section 3.3, we investigated the biological relevance of the patterns uncovered by LAVA based on the UMAP of the KPMP dataset. To do this, we performed overrepresentation analysis (ORA) of biological functions: a statistical method used to determine which functions are statistically overrepresented amongst the functional annotations of the genes in a set of interest (e.g. a LAVA module), compared to what would be expected by chance [54]. We performed this analysis using three collections of functional annotations we thought were relevant for our disease context: (1) hallmark; (2) canonical pathways; and (3) the gene ontology biological process. These collections were downloaded from MSigDB<sup>12</sup>. **Selection of genes per module.** To select the set of genes of interest for ORA, we first summed the correlations of each gene in a module, and then took the set of genes whose sum of correlations was  $\geq 5\%$  of the largest sum (Figure S14). Accordingly, we performed ORA for each module using as background all measured genes from the KPMP dataset (a total of 31332 genes). The resulting biological function  $p$ -values were adjusted using the Benjamini-Hochberg correction for multiple testing. **Results of ORA.** We report the top 50 most significant results of ORA for each of the 9 extracted modules in Figure S15. In the main paper, we highlighted module 4 because of its correlation with diseased samples, and CKD specifically (Section 3.3, Table S2), which we thought was of biological interest.

<sup>12</sup>The Molecular Signatures Database, available at <https://www.gsea-msigdb.org>.

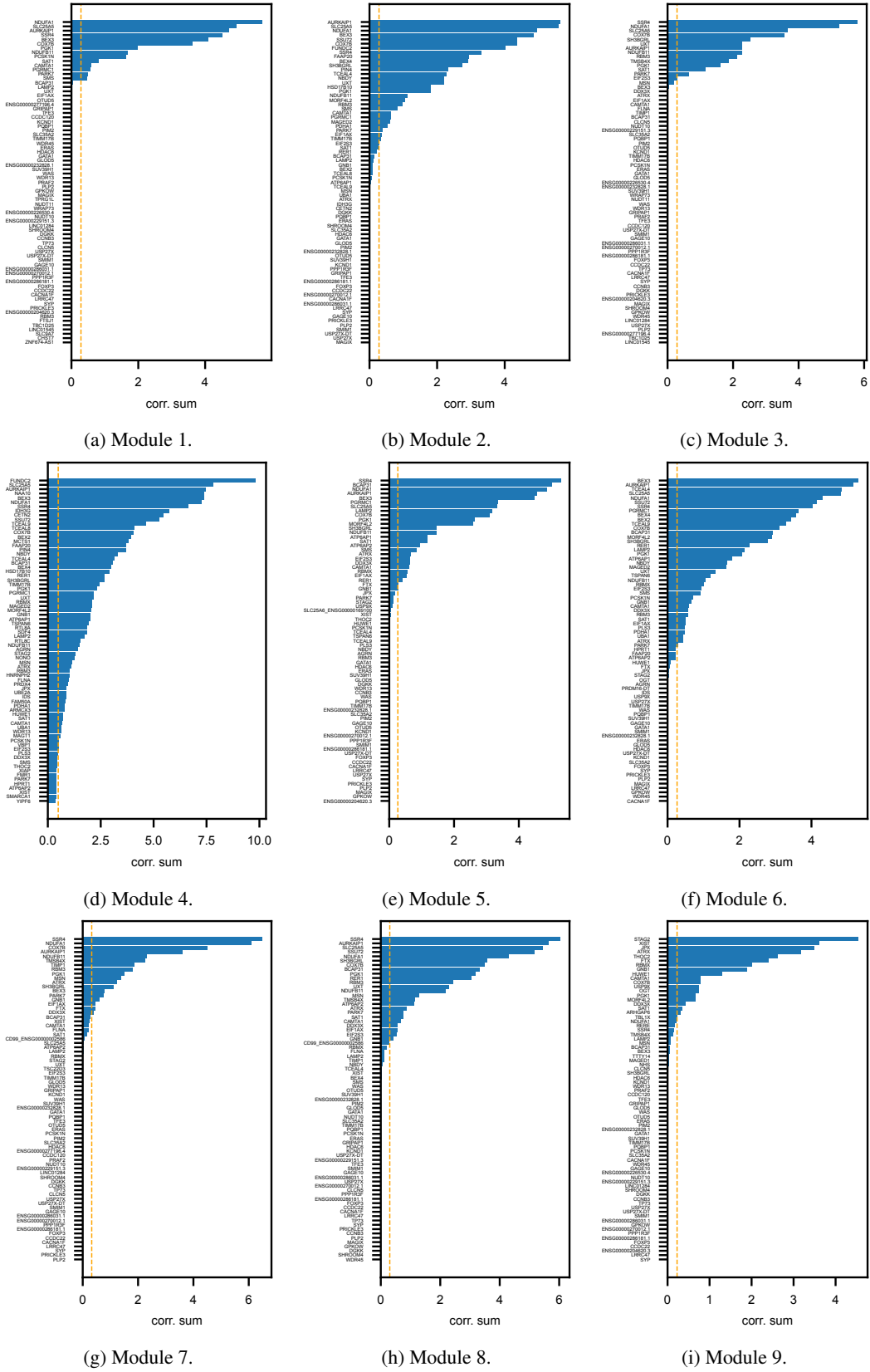


Figure S14: Top 75 genes based on sums of correlations for each extracted module from the KPMP experiments. The orange line represents the cut-off line for gene subsets for ORA, equal to 5% of the largest correlation sum.

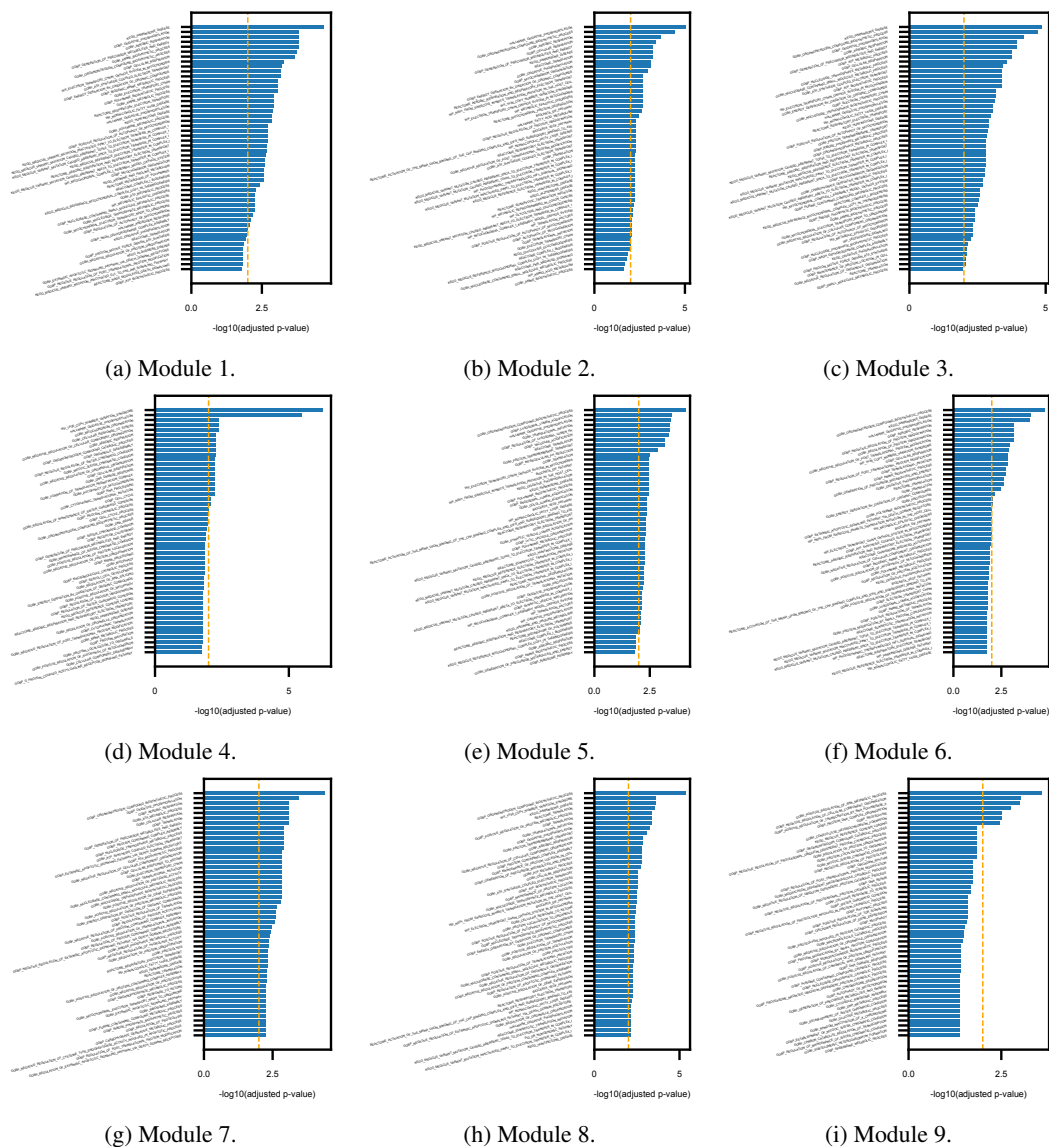


Figure S15: Top 50 most significant pathways based on ORA for each of the 9 extracted modules from the KPMP experiment. The orange line represents the significance  $p$ -value threshold of 0.01, i.e., 2 when looking at  $-\log_{10}(p)$  values.